

Late Afterglow Bump/Plateau around the Jet Break: Signature of a free-to-shocked wind Environment in Gamma-ray Burst

XIAO-YAN LI,¹ DA-BIN LIN,¹ JIA REN,¹ SHU-JIN HOU,^{2,1} YU-FEI LI,¹ XIANG-GAO WANG,¹ AND EN-WEI LIANG¹

¹Laboratory for Relativistic Astrophysics, Department of Physics, Guangxi University, Nanning 530004, China

²College of Physics and Electronic Engineering, Nanyang Normal University, Nanyang, Henan 473061, China

Submitted to ApJ

ABSTRACT

A number of gamma-ray bursts (GRBs) exhibit the late simultaneous bumps in their optical and X-ray afterglows around the jet break. Its origin is unclear. Based on the following two facts, we suggest that this feature may sound a transition of circum-burst environment from a free-wind medium to a homogeneous medium. (I) The late bump followed by a steep decay is strongly reminiscent of the afterglows of GRB 170817A, which is attributed to an off-axis observed external-forward shock (eFS) propagating in an interstellar medium. (II) Observations seem to feature a long shallow decay before the late optical bump, which is different from the afterglow of GRB 170817A. In this paper, we study the emission of an eFS propagating in a free-to-shocked wind for on/off-axis observers, where the mass density in the shocked-wind is almost constant. The late simultaneous bumps/plateaux in the optical and X-ray afterglows are really found around the jet break for high-viewing-angle observers. Moreover, there is a long plateau or shallow decay before the late bump in the theoretical light-curves, which is formed during the eFS propagating in the free-wind. For low-viewing-angle observers, the above bumps appear only in the situation that the structured jet has a low characteristic angle and the deceleration radius of the on-axis jet flow is at around or beyond the free-wind boundary. As examples, the X-ray and optical afterglows of GRBs 120326A, 120404A, and 100814A are fitted. We find that an off-axis observed eFS in a free-to-shocked wind can well explain the afterglows in these bursts.

Keywords: Gamma-ray bursts (629) — Interstellar medium (847) — Interstellar medium wind (848)

1. INTRODUCTION

Gamma-ray bursts (GRBs) are the most luminous sources of electromagnetic radiation known in the Universe. Observationally, GRBs generally appear as a brief and intense γ -rays followed by a long-lived afterglow emission. With the observations of *Swift* satellite, the diversity of light-curves in X-ray afterglows have been revealed (Gehrels et al. 2004; Burrows et al. 2005b). However, a canonical light-curve consisting of four power-law segments and a flaring component has been suggested, i.e., an initial steep decay with a typical slope $\lesssim -3$, a shallow decay with a typical slope ~ -0.5 , a normal decay with a typical slope ~ -1.2 , a late steep decay with a typical slope ~ -2 , and one or several X-ray flares (Zhang et al. 2006; Nousek et al. 2006; O’Brien et al. 2006; Zhang et al. 2007). The initial steep decay component is believed to be the tail of the prompt emission due to the “curvature effect” of the high-latitude emission (Barthelmy et al. 2005; Liang et al. 2006; O’Brien et al. 2006; Lin et al. 2017a,b). The shallow, the normal, and the late steep decays are always attributed to the external shock (Zhang et al. 2006; Nousek et al. 2006; Panaitescu et al. 2006), which is developed when a relativistic jet propagates into the circum-burst medium. If there is no energy injection into the external shock, a normal decay phase would appear in the afterglows. However, the decay may become shallow during the phase with continuous energy injection into the external shock. The late steep decay corresponds to the emission of the external shock after the jet break. The X-ray flares generally show a sharp

rise with a steep decay and thus could not be produced in the external shock (e.g., Romano et al. 2006; Falcone et al. 2006). It is suggested that most of X-ray flares have the same physical origin as the prompt γ -rays (Burrows et al. 2005a; Falcone et al. 2006, 2007; Zhang et al. 2006; Nousek et al. 2006; Liang et al. 2006; Chincarini et al. 2007, 2010; Hou et al. 2014; Wu et al. 2013; Yi et al. 2015, 2016; Mu et al. 2016a,b).

Multi-wavelength observations of afterglows have also revealed some puzzling features, which are beyond the expectation from the simple standard external shock scenario (Panaitescu et al. 2006; Panaitescu & Vestrand 2011; Li et al. 2012; Liang et al. 2013; Wang et al. 2015). For example, some GRBs exhibit late simultaneous bumps in their optical and X-ray afterglows around the jet break, e.g., GRBs 100418A (Marshall et al. 2011; Laskar et al. 2015), 100901A (Gorbovskoy et al. 2012; Laskar et al. 2015), 120326A (Melandri et al. 2014; Hou et al. 2014; Laskar et al. 2015), 120404A (Guidorzi et al. 2014; Laskar et al. 2015). Their optical afterglows seem to feature a long shallow decay before the late bumps. An exemplar of these afterglows is GRB 120326A, which exhibits simultaneous bumps in its optical and X-ray afterglows at around 35 ks after the burst trigger (Urata et al. 2014; Melandri et al. 2014). Hou et al. (2014) propose that a newborn millisecond pulsar with a strong wind is responsible for its late bumps. Melandri et al. (2014) explore various physical scenarios and conclude that the late bumps may be caused by a refreshed external-forward shock or a geometrical effect. By testing various physical processes, Laskar et al. (2015) argue that the energy injection into the external shock is the most plausible mechanism for its late bump. They also argue that GRB 120404A, with optical and X-ray bumps at $t_{\text{obs}} \simeq 1000$ s, can be explained in the same scenario. Guidorzi et al. (2014) attributed the optical/X-ray bumps of GRB 120404A to a decelerating jet viewed close to the jet edge, combined with some early re-energization of the shock. For GRB 100814A, Geng et al. (2016) proposed an ultrarelativistic electron-positron pair wind model to explain the late optical bumps at $t_{\text{obs}} \simeq 10^4$ s. Yu et al. (2015) invoked a magnetar with spin evolution to explain the afterglow emission. Nardini et al. (2014) attributed the feature to the late-time activity of the central engine in the observed afterglow emission. Apart from the late bumps, we also note another puzzling feature that some bursts exhibit late simultaneous plateaux in their optical and X-ray afterglows around the jet break, e.g., GRBs 120729A, 051111, and 070318 (Huang et al. 2018).

The above mentioned late simultaneous bumps/plateaux are all directly followed by a steep decay, which is very different from the decay behavior of afterglows preceding the late simultaneous bumps/plateaux and thus is an intriguing phenomenon. The models involved to explain the late simultaneous bumps/plateaux should also explain the steep decay following the bumps/plateaux. Actually, this feature (i.e., the simultaneous bumps/plateaux directly followed by a steep decay) is strongly reminiscent of the afterglows in GRB 170817A, which is formed in an off-axis observed external-forward shock propagating in an interstellar medium (ISM, Troja et al. 2018; Lamb et al. 2019; Troja et al. 2019; Huang et al. 2019; Ren et al. 2020), of which the mass density is constant. The observations of GRB 170817A reveal an **almost** achromatic bump followed by a steep decay, which is very similar to the GRBs with late bumps mentioned above. Therefore, we would like to suggest that the late simultaneous bumps in GRBs 100814A, 120326A, and 120404A may be formed in an off-axis observed external-forward shock in a homogeneous medium. We would like to point out that the mechanism proposed to explain GRB 170817A has been recently extended to other bursts, e.g., GRBs 080503, 140903A, 150101B, and 160821B (Fraija et al. 2020). Since there is a long shallow decay before the late optical bump in these GRBs, which is different from that of GRB 170817A, the shallow decay may indicate another kind of the circum-burst medium, e.g., the free stellar wind medium.

In this work, we study the emission of the external-forward shock propagating in a free-to-shocked wind circum-burst environment, where the mass density in the shocked wind is almost constant (Weaver et al. 1977; Dyson & Williams 1997; Chevalier & Li 2000). The paper is originated as follows. The dynamics and radiation of the external-forward shock are presented in Section 2. The theoretical afterglows are presented and discussed in Section 3. As examples, we perform the fitting on the X-ray and optical afterglows of GRBs 120326A, 120404A, and 100814A, and the results and discussions are shown in Section 4. The conclusions are summarized in Section 5.

2. DYNAMICS AND RADIATION OF THE EXTERNAL-FORWARD SHOCK

When a relativistic jet propagates in the circum-burst medium of a GRB, an external shock would be developed and thus produces a long-term broadband afterglow emission (Sari et al. 1998; Mészáros & Rees 1999; Sari & Piran 1999a,b). To describe the jet structure and the dynamics of the external-forward shock, we introduce a spherical coordinate (R, θ, φ) with $R = 0$ locating at the burst's central engine and $\theta = 0$ being along the jet axis. The jet flow moving at the direction of (θ, φ) is represented with (θ, φ) -jet. We assume the observer location at the direction of (θ_v, φ_v) with $\varphi_v = 0$ and $\theta_v < \pi/2$.

In our calculations, the jet moving toward us¹ is divided into $I \times L$ small patches along the θ and φ directions in their linear space, i.e., $[0, \delta\theta]$, $[\delta\theta, 2\delta\theta]$, $[2\delta\theta, 3\delta\theta]$, \dots , $[(i-1)\delta\theta, i\delta\theta]$, \dots , $[(I-1)\delta\theta, I\delta\theta]$ with $\delta\theta = \theta_{\text{jet}}/I$ and $[0, \delta\varphi]$, $[\delta\varphi, 2\delta\varphi]$, $[2\delta\varphi, 3\delta\varphi]$, \dots , $[(l-1)\delta\varphi, l\delta\varphi]$, \dots , $[(L-1)\delta\varphi, L\delta\varphi]$ with $\delta\varphi = \pi/L$. Here, θ_{jet} is the opening angle of the jet. The dynamics and the emission of the external-forward shock is estimated independently in each patch. In addition, the following assumptions are adopted in estimating the dynamics and radiation of the external-forward shock: (1) The sideways expansion are ignored and the dynamics at each patch are assumed to be independent of other patches. The amount of sideways expansion is a debated topic, with numerical simulations suggesting a limited amount of spreading (e.g., Granot et al. 2001; Cannizzo et al. 2004; Zhang & MacFadyen 2009; van Eerten et al. 2010; van Eerten & MacFadyen 2012). In addition, it is hard to consider the sideways expansion in the context of a structured jet and the related afterglows fittings. (2) The micro-physical parameters for synchrotron emission, e.g., ϵ_e and ϵ_B , are set as constants, where ϵ_e and ϵ_B are the fractions of the shock energy used to accelerate electrons and contributing to the magnetic energy, respectively. (3) The energy injection in the external shock is not considered in our work.

Circum-burst environment: For massive stars, associated with long GRBs, the stellar wind should be formed and the structure of the wind bubble has been widely studied (e.g., Scalo & Wheeler 2001; Garcia-Segura et al. 1996; Castor et al. 1975). Usually, it is accepted that four regions, i.e., the free stellar wind, the shocked wind, the shocked ISM, and the unshocked ISM, will be formed as the stellar wind interacting with the ISM (Chevalier & Li 2000). Since the latter two regions are too far to reach by the blast wave (please see figure 1 of Chevalier & Li 2000), they are not considered here. The mass density of the stellar wind medium is given by $\rho_{\text{free-wind}} = 5 \times 10^{11} A_* R^{-2} \text{g} \cdot \text{cm}^{-1}$ (Chevalier & Li 2000), where A_* is a constant. However, the mass density in the shocked wind depends on the uncertain physics of the heat conduction. Heat conduction could be prevented by a magnetic field, which is expected to be toroidal in this region (Chevalier et al. 2004). Under this assumption, and using the fact that the internal speed of sound in this region is much higher than the expansion velocity, the density in shocked wind is approximately R -independent and equals to $\xi \rho_{\text{wind}}(R_{\text{tr}})$ with $\xi = 4$ (Weaver et al. 1977; Dyson & Williams 1997; Chevalier & Li 2000). Please see Pe'er & Wijers (2006) for details. Here, R_{tr} , i.e., the free-wind boundary, is the transition radius from the free-wind to the shocked-wind (Kong et al. 2010; Feng & Dai 2011a; Ramirez-Ruiz et al. 2001) and depends on the age of the massive star wind and proper tracking of the shocked medium cooling. In summary, the mass density of the free-to-shocked wind circum-burst environment is described as

$$\rho(R) = \begin{cases} \rho_{\text{free-wind}}(R), & R < R_{\text{tr}}, \\ \rho_{\text{shocked-wind}}(R), & R \geq R_{\text{tr}}, \end{cases} \quad (1)$$

where $\rho_{\text{shocked-wind}} \equiv n_0 m_p \text{cm}^{-3} = \xi \rho_{\text{free-wind}}(R_{\text{tr}})$ and m_p is the proton mass. One should note that the value of ξ can be different from 4. By fitting the afterglows, Jin et al. (2009a) have obtained $\xi \approx 4.07$ for GRB 081109A and Feng & Dai (2011b) have found $\xi = 2.1, 2.0,$ and 2.5 for GRBs 080916C, 080916C, and 090926A, respectively. For simplicity, $\xi = 4$ is adopted in this paper.

Structured jet Description: In this paper, we mainly focus on an axisymmetric structured jet propagating in a free-to-shocked wind circum-burst environment. Our structured jet at the radius R_0 is read as

$$\begin{cases} E_{k,\text{iso}}(\theta, R_0) = E_{k,\text{iso,on}} \exp[-\frac{1}{2}(\frac{\theta}{\theta_c})^2], \\ \Gamma(\theta, R_0) = \Gamma_0, \end{cases} \quad (2)$$

where $E_{k,\text{iso}}/(4\pi)$ is the kinetic energy per solid angle at θ , $E_{k,\text{iso,on}}$ is corresponding to the value of $E_{k,\text{iso}}$ at $\theta = 0$, and θ_c is the characteristic angle of $E_{k,\text{iso}}$.

Dynamics of the external-forward shock: For the (θ, φ) -jet, the evolution of the bulk Lorentz factor $\Gamma(\theta, R)$ is described as (Huang et al. 1999; Huang et al. 2000)

$$\frac{d\Gamma(\theta, R)}{dR} = -\frac{\Gamma^2 - 1}{M_0(\theta) + \epsilon m + 2(1 - \epsilon)\Gamma m} \frac{dm(R)}{dR}, \quad (3)$$

¹ The central engine of a GRB usually launches a pair of outflows, i.e., a near-jet moving toward us and a counter-jet moving away from us. In general, the emission from the counter-jet is negligible compared with the from the near-jet. Then, we only consider the emission from the near-jet.

where $M_0(\theta) = E_{k,\text{iso}}(\theta, R_0)/(4\pi\Gamma_0 c^2)$ with c being the light speed, and m is the sweep-up mass of the external shock from $R_0 = 10^{13}$ cm to R per solid angle and can be estimated with

$$\frac{dm(R)}{dR} = \rho R^2. \quad (4)$$

In Equation (3), $\epsilon(\theta, R) = \epsilon_e \cdot \min[1, (\gamma'_{e,m}/\gamma'_{e,c})^{p-2}]$ is the radiation efficiency of the external-forward shock, where $\gamma'_{e,m} = \epsilon_e(p-2)m_p\Gamma/[(p-1)m_e]$ is the minimum Lorentz factor of the electrons accelerated in the shock, $\gamma'_{e,c} = 6\pi m_e c/(\sigma_T \Gamma B'^2 t_{\text{obs}}^{\text{on}})$ is the efficient cooling Lorentz factor of electrons (Sari et al. 1998). Besides, $B'(\theta, R) = (32\pi\rho\epsilon_B)^{1/2}\Gamma c$ is the magnetic field behind the shock, $t_{\text{obs}}^{\text{on}}(\theta, R) = \int_{R_0}^R (c-v)dr/cv$ with $v(\theta, R) = c\beta$ and $\beta(\theta, R) = \sqrt{1-1/\Gamma^2}$, and m_e , p , and σ_T are the electron mass, the power-law index of accelerated electrons in the shock, and the Thomson cross-section, respectively.

With Equations (1)-(4), one can estimate the value of Γ at different R . Then, the observed time for a photon from (θ, φ) -jet can be estimated with

$$t_{\text{obs}}(\theta, \varphi, \theta_v, R) = (1+z) \left[\frac{R_0}{2\Gamma_0^2 c} + t_{\text{obs}}^{\text{on}} + \frac{R(1-\cos\Theta)}{c} \right], \quad (5)$$

where $\cos\Theta = (\sin\theta\cos\varphi, \sin\theta\sin\varphi, \cos\theta) \cdot (\sin\theta_v, 0, \cos\theta_v) = \sin\theta\cos\varphi\sin\theta_v + \cos\theta\cos\theta_v$, and Θ is the angle between the direction of (θ, φ) and the line of sight, i.e., (θ_v, φ_v) with $\varphi_v = 0$. In Equation (5), the first two terms in the square bracket is the arrival time of photons for an observer being in the direction of (θ_i, φ_i) . Then, if the observer being in the direction of (θ_v, φ_v) with $\varphi_v = 0$, the last term should be added. For a given observer time t_{obs} , one can obtain the corresponding value of $R = R_{\text{obs}}(\theta, \varphi, \theta_v)$ based on Equation (5). The value of R_{obs} is the location of the external-forward shock for the (θ, φ) -jet observed at t_{obs} and is used to calculate the observed flux from the (θ, φ) -jet.

Evolution of the electron energy spectrum: In the X-ray and optical bands, the main radiation mechanism of the external-forward shock in GRBs is the synchrotron radiation of the sweep-up electrons (Sari et al. 1998; Sari & Piran 1999a). We denote the instantaneous electron spectrum for the sweep-up electrons per solid angle in the (θ, φ) -jet as $n'_e(\gamma'_e, \theta, R)$, where $n'_e d\gamma'_e$ is the number of electrons in $[\gamma'_e, \gamma'_e + d\gamma'_e]$ with γ'_e being the Lorentz factor of electrons. The evolution of n'_e can be described as

$$\frac{\partial n'_e}{\partial t'} + \frac{\partial}{\partial \gamma'_e} (\dot{\gamma}'_e n'_e) = Q', \quad (6)$$

where $\dot{\gamma}'_e$ is the cooling rate of electrons and Q' is the injection rate of electrons from the shock, i.e.,

$$\dot{\gamma}'_e(\gamma'_e, \theta, R) \equiv \frac{d\gamma'_e}{dt'} = -\frac{\sigma_T \gamma'^2_e B'^2}{6\pi m_e c} - \frac{2}{3} \frac{\gamma'_e}{R} \frac{dR}{dt'}. \quad (7)$$

$$Q'(\gamma'_e, \theta, R) = \begin{cases} Q'_0 \gamma'^{-p}_e, & \gamma'_{e,m} \leq \gamma'_e \leq \gamma'_{e,\text{max}}, \\ 0, & \text{others,} \end{cases} \quad (8)$$

Here, $p(>2)$ is the power-law index, $\gamma'_{e,\text{max}} = \sqrt{9m_e^2 c^4 / (8B' q_e^3)}$ with q_e being the electron charge (e.g., Kumar et al. 2012), Q'_0 is obtained by solving $\int_{\gamma'_{e,m}}^{\gamma'_{e,\text{max}}} Q' d\gamma'_e = (R^2 \rho / m_p) dR/dt'$ with $dR/dt' = c\beta\Gamma$, and $t'(\theta, R)$ is the time elapsed in the comoving frame of the blast wave. The first and second terms in the right-hand side of Equation (7) are respectively the synchrotron radiative cooling and adiabatic cooling of electrons, and the inverse-Compton cooling is not considered here. We solve Equation (6) and $dR/dt' = c\beta\Gamma$ for $n'_e(\gamma'_e, \theta, R)$ at different R . In our calculations, the fourth-order Runge-Kutta method is used. In addition, an appropriate time step $\Delta t' < \min\{\Delta\gamma'_e/\dot{\gamma}'_e\}$ is adopted in our calculations, where $\Delta\gamma'_e$ is the width of our adopted energy grids for electrons (e.g., see appendix A of Geng et al. 2018).

Observed flux calculation: With the obtained $n'_e(\gamma'_e, \theta, R)$, the spectral power of synchrotron radiation at a given frequency ν' can be described as

$$P'(\nu', \theta, R) = \frac{\sqrt{3}q_e^3 B'}{m_e c^2} \int_0^{\gamma'_{\text{max}}} F(\nu'/\nu'_{\text{syn}}) n'_e(\gamma'_e, \theta, R) d\gamma'_e, \quad (9)$$

where $F(x) = x \int_x^{+\infty} K_{5/3}(k) dk$ with $K_{5/3}(k)$ being the modified Bessel function of 5/3 order and $\nu'_{\text{syn}} = 3q_e B'(\theta, R) \gamma_e'^2 / (4\pi m_e c)$. Then, the observed flux density $\hat{f}_\nu(\theta, R)$ from the per solid angle of the jet flow in the direction of (θ, φ) is

$$\hat{f}_\nu(\theta, \varphi, \theta_v, R) = (1+z) P' \left(\nu \frac{1+z}{D}, \theta, R \right) D^3 \frac{1}{4\pi d_L^2}, \quad (10)$$

where ν is the observed photon frequency, d_L is the luminosity distance at the cosmological redshift z , and $D(\theta, \varphi, \theta_v, R) = 1/[\Gamma(1 - \beta \cos \Theta)]$ is the Doppler factor of the (θ, φ) -jet relative to the observer. Then, the observed total flux density f_ν at t_{obs} is

$$f_\nu(t_{\text{obs}}) = 2 \sum_{i=1}^I \sum_{l=1}^L \hat{f}_\nu(\theta_i, \varphi_l, \theta_v, R_{\text{obs}}) \sin \theta_i \delta\theta \delta\varphi, \quad (11)$$

where $\theta_i = (i - 0.5)\delta\theta$ and $\varphi_l = (l - 0.5)\delta\varphi$. The observed flux F_{XRT} in the X-ray band (0.3 – 10 keV) of the X-ray telescope (XRT) aboard *Swift* satellite is calculated with $F_{\text{XRT}} = \int_{\nu_{0.3}}^{\nu_{10}} f_\nu(t_{\text{obs}}) d\nu$, where $h\nu_{10} = 10$ keV and $h\nu_{0.3} = 0.3$ keV.

3. THEORETICAL AFTERGLOWS

In this paper, we mainly focused on the afterglows of GRBs in a free-to-shocked wind circum-burst environment. In Figure 1, we shows the light-curves (solid lines) of the radiation from the external-forward shock propagating in a free-to-shocked wind circum-burst environment, where $E_{k,\text{iso,on}} = 10^{52}$ erg, $\Gamma_0 = 250$, $\theta_c = 5^\circ$, $\theta_{\text{jet}} = 8\theta_c$, $p = 2.2$, $\epsilon_e = 0.1$, $\epsilon_B = 10^{-4}$, $A_* = 0.01$, $R_{\text{tr}} = 10^{17}$ cm, and $z = 1$ are adopted to calculate the dynamics and emission of the external-forward shock². One can find that the XRT/optical light-curves (solid lines) from a low viewing angle (e.g., $\theta_v \lesssim \theta_c$) can be decomposed into three phases: (i) the free-wind-phase, which appears in the early stage and is formed during the external-forward shock propagating in the free-wind environment; (ii) the shocked-wind-phase, which appears in the middle section bridging the free-wind-phase to the post-jet-break-phase and is formed during the external-forward shock propagating in the uniform shocked-wind environment; (iii) the post-jet-break-phase, which appears in the late stage as a steep decay by reflecting the situation that the jet core is fully visible for the observer, i.e., $\Gamma(\theta_c, R) \cdot \sin(\theta_c + \theta_v) \lesssim 1$ ³. Here, $\Gamma(\theta_c, R)$ is the bulk Lorentz factor of the jet flow in the direction with $\theta = \theta_c$, θ_c is the characteristic angle of $E_{k,\text{iso}}$, and the direction of (θ_v, φ_v) with $\varphi_v = 0$ is the line of sight.

Figure 1 reveals that the transition from a free-wind to a homogeneous shocked-wind generally witnesses the flattening/brightening of the light-curves. By increasing the viewing angle, the changes in light-curves of Figure 1 (solid lines) can be summarized as follows. (1) Firstly, the free-wind-phase and the shocked-wind-phase become shallow while the post-jet-break phase remains its morphology. (2) At a certain viewing angle, e.g., $\theta_v \sim 4\theta_c$, the late simultaneous plateaux in the optical and X-ray afterglows appear. It should be pointed out that these plateaux are all directly followed by a post-jet-break-phase, which is similar to the late plateau found in the afterglows of GRBs 120729A, 051111, and 070318 (Huang et al. 2018). (3) Further increasing the viewing angle, the free-wind-phase turns into a rising pattern. Meanwhile, the free-wind-phase and post-jet-break-phase remain their decaying morphology. Then, the late simultaneous bumps in the optical and X-ray afterglows appear. It should be pointed out that these late bumps are directly followed by a post-jet-break-phase and preceded by a shallow decay, which is very similar to the late simultaneous bumps found in some bursts, e.g., GRBs 100418A, 100901A, 120326A, and 120404A. The behaviors of (2) and (3), i.e., the late simultaneous bumps/plateaux followed by a post-jet-break-phase in the optical and X-ray afterglows, are the key findings of this work. In Figure 2, we also shows X-ray afterglows (solid lines) of the external-forward shock in a free-to-shocked wind environment for a jet with $\theta_{\text{jet}} = \theta_c$, where the values of the other parameters are the same as those in Figure 1. One can find that the free-wind-phase in Figure 2 is shallower than that in Figure 1 for the light-curves from large viewing angles. Then, the opening angle of the jet may affect the light-curves before the late bump/plateau. It is worthy to point out that the only difference in producing the light-curves of Figure 1 or

² In general, the value of $A_* \sim 1$ is assumed. However, the value of $A_* < 1$ is generally reported in fitting the afterglows of GRBs, e.g., $A_* \simeq 0.005 - 0.032$ for GRB 050319 (Kamble et al. 2007), $A_* \simeq 0.02$ for GRB 081109A (Jin et al. 2009b), $A_* \simeq 0.2$ for GRB 160625B (Fraija et al. 2017), and $A_* \simeq 0.06$ for GRB 190114C (Fraija et al. 2019). Since the value of $A_* \sim 0.01$ is obtained from these fittings, $A_* \sim 0.01$ is adopted to discuss the theoretical light-curves for an external-forward shock propagating in a free-to-shocked wind circum-burst environment.

³ For a low value of $\theta_c + \theta_v$, $\Gamma_c \cdot \sin(\theta_c + \theta_v)$ is reduced to $\Gamma_c \cdot (\theta_c + \theta_v)$, which is generally used in discussing the jet-break behavior. For a high value of $\theta_c + \theta_v$, however, the jet-break appears in the situation with $\Gamma_c \cdot \sin(\theta_c + \theta_v) \sim 1$ rather than $\Gamma_c \cdot (\theta_c + \theta_v) \sim 1$.

2 is the viewing angle θ_v . Thus, the appearance of the late simultaneous bumps/plateaux in Figure 1 or 2 is related to the differences in the viewing angle rather than in the dynamics of the external shock.

For the structured jet adopted in Figures 1 and 2, the deceleration radius of the on-axis jet flow is in the free-wind medium, where the deceleration radius of the (0, 0)-jet is 1.17×10^{14} cm based on Equation (A4). Then, there is no broad late bumps in the afterglows for an on-axis observer. In fact, the late simultaneous bumps/plateaux appear only in the cases with high viewing angle for the free-to-shocked-wind-afterglows of Figure 1 or 2. We would like to point out that if the deceleration radius of the on-axis jet flow lies beyond or at around the free-wind boundary, a broad bump preceded by a long plateau or shallow decay can appear in the afterglows even in the cases with low viewing angle. In Figure 3, we shows the light-curves of the radiation from the external-forward shock propagating in a free-to-shocked wind environment, where a structured jet with $E_{k,iso,on} = 10^{55}$ erg, $\Gamma_0 = 100$, $\theta_{jet} = 8\theta_c$, $p = 2.2$, $\epsilon_e = 0.1$, $\epsilon_B = 10^{-4}$, $A_* = 0.01$, $R_{tr} = 10^{17}$ cm, and $\theta_c = 5^\circ$ (top panel) or $\theta_c = 0.5^\circ$ (bottom panel) is adopted. For the given structured jet in Figure 3, the deceleration radius of the (0, 0)-jet in the free-wind medium is 7.33×10^{17} cm, which is significantly larger than R_{tr} . Then, the deceleration radius of the on-axis jet flow would lie beyond the free-wind boundary. In Figure 3, late broad bumps preceded by a long plateau or shallow decay indeed appear in the afterglows for the cases with low viewing angle. In addition, the late broad bump is followed by a normal/steep decay if a structured jet with high/low characteristic angle θ_c (e.g. $\theta_c = 5^\circ/\theta_c = 0.5^\circ$) is adopted.

Now, we can conclude that the late simultaneous broad bumps directly followed by a steep decay and preceded by a long plateau or shallow decay may sound the external-forward shock propagating in a free-to-shocked wind environment. In addition, one of the following conditions should be satisfied: ① the observer should have a high viewing angle with respect to the jet axis; ② the structured jet should have a low characteristic angle and the deceleration radius of the on-axis jet flow is at around or beyond the free-wind boundary. The reason for the appearance of the broad bumps in condition ② or Figure 3 is clear. However, the reason for the appearance of the bumps/plateaux in condition ① or Figures 1 and 2 is unclear. Then, the following subsections, i.e., Subsection 3.1-3.3, are dedicated to discuss the late simultaneous bumps/plateau in Figures 1 and 2.

3.1. Understanding the Appearance of Late bump/plateau

The appearance of the bump/plateau in Figure 1 or 2 can be understood as follows. In Figures 1 and 2, we also plot the afterglows formed in a pure free-wind medium with $\rho = 5 \times 10^{11} A_* R^{-k} g \cdot \text{cm}^{-3}$ (dotted lines) and those formed in a pure shocked-wind medium with $\rho = n_0 m_p \text{cm}^{-3}$ (dashed lines) for some viewing angles. (Hereafter, the afterglow formed in a free/shocked/free-to-shocked wind environment is represented with “free/shocked/free-to-shocked-wind-afterglow”.) One can find that the light-curves of the shocked-wind-phase and the post-jet-break-phase are almost the same as those of the shocked-wind-afterglow in the same time interval. Then, the afterglow formed in a free-to-shocked wind environment can be approximately estimated by superposition of the free-wind-afterglow and the shocked-wind-afterglow from different viewing angle. By increasing the viewing angle, the decay of the free-wind-afterglows and the shocked-wind-afterglows become shallow. Then, the free/shocked-wind-phase in the free-to-shocked-wind-afterglows become shallow correspondingly. Similar to the afterglow of GRB 170817A, a late bump followed by a post-jet-break phase is presented in the shocked-wind-afterglow while it is viewed at a large viewing angle, e.g., $\theta_v \gtrsim 4\theta_c$. However, the free-wind-afterglow remains its decaying pattern before the late bump of the shocked-wind-afterglow. Then, a late bump/plateau followed by a post-jet-break-phase and preceding by a plateau/shallow decay emerges by superposition of the free-wind-afterglow and the shocked-wind-afterglow. This is the phenomenological reason for the appearance of the late bump/plateau.

In this paragraph, we discuss the morphology of the free/shocked-wind-afterglows for high-viewing-angle observers. For the sake of discussion, we first study the morphology of the free/shocked-wind-afterglows for a top-hat jet. In Appendix A.3, the analytical results of the free/shocked-wind afterglow for a top-hat jet are derived and summarized in Table 2. It can be found that high-viewing-angle observers generally witnesses a rising pattern before the post-jet-break-phase for the afterglows from a top-hat jet. Besides, the rise of the free-wind-afterglow is gentle compared with the rise of the shocked-wind-afterglow, of which the rising power-law index $-\alpha$ is larger than 4. This behavior can be found in Figure 2, where a Gaussian structured jet with $\theta_{jet} = \theta_c$ describes a top-hat jet approximately. For high-viewing-angle observers (e.g., $\theta_v > \theta_c$), Figure 2 reveals that the rising power-law index $-\alpha$ is around 0.5 in the free-wind afterglows and is around 4 in the shocked-wind afterglows. Correspondingly, the free-wind afterglows appear as an extremely wide bump with a slow rise, and the shocked-wind afterglows appear as a narrow bump with a fast rise. These results are consistent with those summarized in Table 2. In Figure 4, we shows the free-to-shocked-wind-

afterglows for a Gaussian structured jet with different θ_{jet} , where $\theta_v = 4\theta_c$ is set. One can find that the emission of the jet core mainly makes its contribution to the afterglow around the jet break for high-viewing-angle observers, and the emission of the jet flow being close to the line of sight dominates the early phase of afterglow. Figure 4 also reveals that the superposition of the emission from the jet flow being close to the line of sight to the emission of the jet core generally slows down the rise of the early afterglows, and even changes the rising pattern into the decaying pattern for the early afterglows. Then, there is a long plateau or shallow decay before the late bump in our theoretical light-curves.

3.2. Characteristic Transition Time

The free-to-shocked afterglows have two characteristic transition time: the transition from free-wind phase to the shocked-wind-phase (named as “the first-transition” in this paper); the transition from the shocked-wind-phase to the post-jet-break-phase (named as “the second-transition” in this paper).

The first-transition may be related to the observed time of the jet flow crossing R_{tr} . This can be found by comparing the light-curves in Figure 4 for the situations with $\xi = 4$ (solid lines), $\xi = 16$ (dotted lines), $\xi = 64$ (dashed lines), where the values of A_* and n_0 are respectively the same in different situations, and the value of R_{tr} is changed in order to obtain different $\xi = \rho_{\text{shocked-wind}}/\rho_{\text{free-wind}}(R_{\text{tr}})$. The increase of ξ in Figure 4 is related to the increase of R_{tr} . Figure 4 reveals that a higher value of R_{tr} adopted, a later of first-transition appears. In Figure 1, we plot the observed times of the (θ_v, φ_v) -jet and $(0, 0)$ -jet⁴ crossing R_{tr} with “●” and “○” symbols, respectively. (Hereafter, the symbols and lines with a same color in a same figure corresponds to the situation with a same viewing angle.) One can find that the first-transition occurs during the (θ_v, φ_v) -jet crossing R_{tr} for low-viewing-angle observers. For high-viewing-angle observers, however, the time for the (θ_v, φ_v) -jet crossing R_{tr} is significantly larger than the first-transition time. This implies that the free-wind-phase is shaped by the emission of the jet flow at around $(\theta, \varphi)=(\theta_v, \varphi_v)$ only in the situations with low viewing angle. Figure 1 also reveals that the observed time of the $(0, 0)$ -jet crossing R_{tr} , i.e., the “○” symbols, is generally larger than the first-transition time. Then, we can believe that the first-transition is not associated with the dynamics of the (θ_v, φ_v) -jet or $(0, 0)$ -jet for high-viewing-angle situations. In Figure 4, the first-transition occurs later by decreasing θ_{jet} . Then, one can believe that the first-transition should be related to the dynamics of the jet flow being in the direction between (θ_v, φ_v) and $(0, 0)$ directions. We have found that the observed times of the $(2\theta_c, \varphi_v)$ -jet and $(3\theta_c, \varphi_v)$ -jet crossing R_{tr} are at around the first-transition for the situations with $\theta_v = 4\theta_c$ and $\theta_v = 8\theta_c$, respectively.

The second-transition from the shocked-wind-phase to the post-jet-break-phase may be related to the following three observed times⁵: (i) the near core-edge, i.e., (θ_c, φ_v) -jet, begins to be visible for the observer, i.e., $\Gamma(\theta_c, R) \sin(\theta_v - \theta_c) \simeq 1$; (ii) the jet axis, i.e., $(0, 0)$ -jet, begins to be visible for the observer, i.e., $\Gamma(0, R) \sin(\theta_v) \simeq 1$; (iii) the far core-edge, i.e., $(\theta_c, \varphi_v + \pi)$ -jet, begins to be visible for the observer, i.e., $\Gamma(\theta_c, R) \sin(\theta_v + \theta_c) \simeq 1$. It is worthy to point out that when the far core-edge becomes visible, the afterglow fully enters into the post-jet-break phase and appears as a steep decay. In Figures 1 and 2, the observed times of (i), (ii), and (iii) are indicated with “▷”, “◊”, and “◁” symbols, respectively. It can be found that the second-transition begins at around “▷” and ends at “◁” for an observer with low viewing angle. In addition, the “▷” symbols are generally at around the end of the plateau or the peak of the bump if the late bump/plateau appears in the afterglows. For high-viewing-angle observers, the shocked-wind-phase generally appears as a plateau or fast rise. Then, the second-transition begins at the end of the plateau or fast rise, i.e., the observed time of the “▷” symbols, for high-viewing-angle observers. In summary, the second-transition begins at around “▷” and ends at “◁”.

3.3. Behaviors of the Late Bump/Plateau

We note that the energy injection into the external shock is always used to explain the bump/plateau in the afterglows. In the energy injection scenario, it is worthy to point out that the light-curve of the afterglow shaped by the energy injection is achromatic⁶. However, we find that the free-to-shocked-wind-afterglows from an off-axis

⁴ The $(0, 0)$ -jet represents the jet flow along the jet axis. For a high-viewing-angle observer, the observed time of the $(0, 0)$ -jet crossing R_{tr} can be analytically estimated with Equation (A2), i.e., $t_{\text{obs}}(0, 0, \theta_v, R_{\text{tr}}) = (1+z)(1 - \cos \theta_v)R_{\text{tr}}/c$, which is consistent with that obtained based on the numerical method (i.e., “○” symbols in Figure 1).

⁵ If $\Gamma_0 \gg 1/\sin(\theta_v - \theta_c)$ is satisfied, the observed time of (i), (ii), and (iii) can be analytically estimated with $[\sin(\theta_v - \theta_c)]^{-\frac{\varepsilon+2s-8}{3-s}} \Gamma_0^{-\frac{\varepsilon+2s-8}{3-s}} \zeta t_{\text{dec}}$, $[\sin \theta_v]^{-\frac{\varepsilon+2s-8}{3-s}} \Gamma_0^{-\frac{\varepsilon+2s-8}{3-s}} \zeta t_{\text{dec}}$, and $[\sin(\theta_v + \theta_c)]^{-\frac{\varepsilon+2s-8}{3-s}} \Gamma_0^{-\frac{\varepsilon+2s-8}{3-s}} \zeta t_{\text{dec}}$ based on Equation (A1), respectively. The analytical results of above three observed times are consistent with these estimated based on numerical method, i.e., the values shown with “▷”, “◊”, and “◁” symbols in Figures 1 and 2.

⁶ The energy injection model is always used to explain the simultaneous bumps/plateaux in the afterglows. In this scenario, the rise of the bumps is generally shaped by the energy injection and thus is achromatic. However, the decay of bumps in different bands may not follow a same morphology since the decay phase of bumps is generally not shaped by the energy injection.

observed structured jet does not present an absolutely achromatic bump/plateau. In Figure 5, we show the afterglows observed in the radio-band ($\nu = 10\text{GHz}$, dotted lines), R -band (dashed lines), and XRT band (solid lines) for the situation with $\theta_v = 2\theta_c$ (blue lines), $3\theta_c$ (orange lines), $4\theta_c$ (magenta lines) or $8\theta_c$ (violet lines). One can find that the bumps/plateaux in the radio, optical, and X-ray afterglows are simultaneous but not absolutely achromatic, especially for the situations with low viewing angle. This behavior is different from that of the bump/plateau formed in the energy injection scenario. The different behavior of simultaneous bumps/plateaux in the afterglows from the energy injection scenario and those from our scenario (i.e., an off-axis observed structured jet propagating in a free-to-shocked wind environment) can be understood as follows. The energy injection scenario and our scenario may be not fundamentally different in shaping the simultaneous bumps/plateaux because both scenarios try to account for light-curve morphology by varying the kinetic energy of the visible jet flow. In the energy injection scenario, the kinetic energy varies in the lab and observer time owing to the energy injection into the external shock. In our scenario, the kinetic energy of the visible jet flow implicitly varies with observer time since the observer sees an increasing region of the structured jet owing to the deceleration of the jet. However, the observed flux in our scenario involves the emission from all of visible region of the structured jet rather than that only from the region being just right visible. Then, the appearance of bump or plateau may be simultaneous but not absolutely achromatic in different observed bands. Since our obtained bumps/plateaux appear simultaneous in the optical and X-ray afterglows, our scenario could not fully account for chromatic bumps/plateaux.

In Figure 6, we show the free/shocked/free-to-shocked-wind-afterglows for a jet with $\theta_c = 0.5^\circ$, where the values of other parameters are the same as those in Figure 1. One can find that the width of late bump/plateau in Figure 6 is narrower than that in Figure 1. It reveals that the characteristic angle θ_c of the structured jet may affect the width of the late bump/plateau for the cases with a same θ_v/θ_c . The reason is presented as follows. In Figures 1 and 2, the peak time of bump or the end of plateau is close to the beginning of the post-jet-break-phase. In addition, the free-wind boundary is reached well before the post-jet-break-phase for an on-axis observer (i.e., $\theta_v = 0$) and thus for an off-axis observer. Then, one can find a broad bump/plateau for an observer with high viewing angle. In Figure 6, one can find that the free-wind boundary is reached during the post-jet-break-phase for an observer with low viewing angle (e.g., $\theta_v \lesssim 2\theta_c$), and is reached just before the post-jet-break-phase for an observer with high viewing angle (e.g., $\theta_v \gtrsim 4\theta_c$). Then, one can find a narrow bump/plateau. By summary up the light-curves in Figures 1, 2, and 6, one can conclude that the late simultaneous broad bumps (e.g., GRB 120326A) only appear in the situation that the free-wind boundary is reached well before the jet core becomes fully visible for an observer with high viewing angle.

4. CASE STUDY

As examples, we perform the fitting on the X-ray and optical afterglows of GRBs 120326A, 120404A, and 100814A. The light-curves from prompt emission to the late afterglow of these bursts are shown in Figure 5, where the late bumps directly followed by a post-jet-break-phase and preceded by a plateau or shallow decay can be easily found in these light-curves.

- GRBs 120326A is a long GRB at redshift $z = 1.798$ with unusual X-ray and optical afterglows. The late simultaneous bumps followed by a post-jet-break-phase in the optical and X-ray afterglows can be easily found at around $t_{\text{obs}} \sim 4 \times 10^4$ s. Some authors proposed that the energy injection model may be responsible to this late bump (e.g., Melandri et al. 2014; Hou et al. 2014; Laskar et al. 2015). Since the observed bumps is very similar to those found in Figures 1-3, we would like to model the late simultaneous bumps based on an off-axis observed external-forward shock in a free-to-shocked wind environment. The XRT data at $t_{\text{obs}} \gtrsim 3 \times 10^3$ s and the optical data at $t_{\text{obs}} \gtrsim 10^2$ s are used in our fitting.
- GRB 120404A, with redshift $z = 2.876$, is a long GRB with a significant rebrightening in the optical and near-infrared bands at $t_{\text{obs}} \sim 2 \times 10^3$ s. The X-ray observations around this time also show a bump although the data are sparse owing to the orbital gap of *Swift* (Guidorzi et al. 2014). Interestingly, the bumps are all directly followed by a post-jet-break-phase. Laskar et al. (2015) proposed that the energy injection model may be responsible to this late bump. However, we would like to model these two late simultaneous bumps based on an off-axis observed external-forward shock in a free-to-shocked wind environment since these bumps are similar to those in Figures 1-3. The XRT data at $t_{\text{obs}} > 550$ s and the optical data at $t_{\text{obs}} \gtrsim 200$ s are used for our fitting.

- GRB 100814A is a long GRB with the redshift $z = 1.44$. The optical rebrightening appears at 10^5 s. De Pasquale et al. (2015) presented a broadband observations of GRB 100814A and they attribute the late optical rebrightening to a long-lived external-reverse shock and external-forward shock. Besides, Geng et al. (2016) used an ultrarelativistic e^+e^- wind injection model to explain the late rebrightening. It should be noted that the optical/X-ray afterglows all turn into the steep decay after the peak time of the optical bump. Then, we would like to believe that there may be a simultaneous late bumps in the optical and X-ray afterglows and the rise of the X-ray bump is covered by the late central engine activities. The XRT data at $t_{\text{obs}} \gtrsim 9 \times 10^4$ s and the optical data at $t_{\text{obs}} \gtrsim 10^3$ s are also modelled as the emission from an off-axis observed external-forward shock in a free-to-shocked wind environment.

Our fitting is performed based on the Markov Chain Monte Carlo (MCMC) method to produce posterior predictions for the model parameters. MCMC method is widely used in finding a best set of parameters for a specified model, e.g., GRB 080413B (Geng et al. 2016); GRBs 100418A, 100901A, 120326A, and 120404A (Laskar et al. 2015). In our work, fitting the afterglows of GRBs 120326A, 120404A, and 100814A with the MCMC method is to test whether or not the late simultaneous bumps followed by a post-jet-break-phase can be explained with an off-axis observed external-forward shock in a free-to-shocked wind environment. The posterior probability density functions for the physical parameters, i.e., $E_{k,\text{iso,on}}$, Γ_0 , θ_c , $\theta_{\text{jet}}/\theta_c$, θ_v/θ_c , p , ϵ_e , ϵ_B , A_* , and R_{tr} , are presented in Figure 8, where only the fitting result of GRB 120326A is shown as an example. The optimal result from MCMC fitting is shown in Figure 7 with blue line (XRT) and red line (optical), and the obtained parameters at the 1σ confidence level are reported in Table 1, where the values of the transition radius R_{tr} (i.e., $1.05 \times 10^{17}\text{cm}$, $6.31 \times 10^{16}\text{cm}$, and $3.98 \times 10^{17}\text{cm}$ for GRBs 120326A, 120404A and 100814A, respectively) are consistent with those found in other bursts (e.g., Kong et al. 2010; Feng & Dai 2011a; Ramirez-Ruiz et al. 2001; Li et al. 2020). It can be found that both the X-ray afterglow and the optical afterglow of these bumps can be well modelled with an off-axis observed external-forward shock in a free-to-shocked wind environment.

1. The fitting results reported in Table 1 reveals that the on-axis observed isotropic kinetic energy $E_{k,\text{iso,on}}$ of these bursts (i.e., $\sim 5 \times 10^{54}\text{erg}$, $6 \times 10^{53}\text{erg}$, and $8 \times 10^{54}\text{erg}$ for GRBs 120326A, 120404A, and 100814A, respectively) are significantly high but consistent with those found in other bursts (see the figure 10 in Racusin et al. 2011 and the table 1 in Yi et al. 2017). The total kinetic energy of the structured jet is also estimated and shown in the last row of Table 1. Compared with the beaming corrected kinetic energy reported in the table 2 of Yi et al. (2017), the total kinetic energy of our obtained structured jet is also consistent with those found in other bursts. However, it should be noted that the on-axis observed luminosity of GRBs 120326A and 100814A may be significantly high since the value of $\theta_v \sim 4\theta_c$ is obtained from our MCMC fittings. According to the structure of the jet, the on-axis observed luminosity of these two bursts may be around $10^{54}\text{erg} \cdot \text{s}^{-1}$, which lies in the high-luminosity range of GRBs. Here, the time-averaged luminosity of GRBs 120326A and 100814A are estimated to be around $\sim 2 \times 10^{51}\text{erg} \cdot \text{s}^{-1}$ (Melandri et al. 2014) and $10^{51}\text{erg} \cdot \text{s}^{-1}$ (Nardini et al. 2014), respectively.
2. The theoretical light-curves does not well fit the transition behavior from the wind-phase to the ISM-like phase in the afterglows of GRB 120326A. It may imply that the density jump factor ξ from the wind medium to the ISM-like medium may be less than 4, i.e., $\xi < 4$. Figure 1 reveals that the external-forward shock propagating in a shocked-wind environment can yield a plateau before the late simultaneous bumps in the case with $\theta_v = 4\theta_c$. Then, we try to fit the afterglows of GRB 120326A with the emission of the external-forward shock propagating in a homogeneous medium, where the priors of $\log_{10}(E_{k,\text{iso,on}}/\text{erg})$, $\log_{10}\Gamma_0$, θ_c , $\theta_{\text{jet}}/\theta_c$, θ_v/θ_c , p , $\log_{10}\epsilon_e$, $\log_{10}\epsilon_B$, and $\log_{10}n_0$ are set as uniform distribution in the range of (52, 55), (1.5, 3.0), (0.3, 8.0), (2.5, 4.5), (0.0, 8.0), (2.1, 2.9), (-3.2, -0.5), (-6.5, -2.0), and (0.0, 1.7) in our MCMC fittings, respectively. However, no well fitting result is found. The fitting result with minimum reduced χ^2 is shown with dashed lines in the top panel of Figure 7. It can be found that the early plateau of GRB 120326A could not be well fitted based on the emission of the external-forward shock in a homogeneous medium.
3. There seems to be a plateau at $t_{\text{obs}} \sim 600$ s in the optical afterglow of GRB 100814A, which may indicate an energy injection into the external shock. If so, our model could not well describe the afterglows of GRB 100814A in its early phase. This may be the reason for the deviation of our theoretical results relative to the observations in the early phase. In addition, the X-ray and optical afterglows of GRB 100814A show a chromatic behavior,

which could not be explained only with our scenario (i.e., an off-axis observed structured jet propagating into a free-to-shocked wind environment) since the appearance of the late simultaneous bump/plateau in our scenario is quasi-achromatic. Other emission rather than that of the external-forward shock may contribute to the long X-ray shallow decay.

4. For the afterglows of GRB 120404, the fitting result shows that the line of sight lies within the jet core, i.e., $\theta_v = 0.68\theta_c$. However, the late simultaneous bumps do not appear in the free-to-shocked-wind-afterglows of Figures 1 and 2 for $\theta_v < \theta_c$. Then, the appearance of the bumps in GRB 120404 should be related to the condition ②, i.e., the structured jet has a low characteristic angle and the deceleration radius of the on-axis jet flow is at around or beyond the free-wind boundary. Based on the fitting result of this burst, the deceleration radius of the (0, 0)-jet can be estimated and is 2.43×10^{16} cm, which is at around the transition radius $R_{tr} = 6.31 \times 10^{16}$ cm of this burst. Then, the fitting result is consistent with the condition ②.

5. CONCLUSION

In this paper, the emission of the external-forward shock in a free-to-shocked wind circum-burst environment is studied. We mainly focus on the light-curves of the afterglows in the late phase. A late simultaneous broad bumps/plateaux followed by a post-jet-break-phase and preceded by a plateau or shallow decay is found in the obtained afterglows with one of the following conditions: ① the observer should have a high viewing angle with respect to the jet axis; ② the structured jet should have a low characteristic angle and the deceleration radius of the on-axis jet flow is at around or beyond the free-wind boundary. Our obtained bump/plateau in the afterglows is similar to those found in the afterglows of some bursts, e.g., the late bump found in GRBs 100418A, 100901A, 120326A, 120404A (see Laskar et al. 2015), 080413B, 091029, 100814A, and 090426 (see Geng et al. 2016), and the late plateau found in GRBs 120729A, 051111, and 070318 (see Huang et al. 2018). As examples, we perform the fitting on the optical and X-ray afterglows of GRB 100814A, GRB 120326A and GRB 120404A based on the Markov Chain Monte Carlo method. It is found that the external-forward shock propagating in a free-to-shocked wind circum-burst environment for an off-axis observer can well explain the late phase of the optical and X-ray afterglows in these bursts. Since our obtained bumps/plateaux appear simultaneous in the optical and X-ray afterglows, our scenario could not fully account for chromatic bumps/plateaux, e.g., GRB 100814A. Then, we suggest that a late broad bump/plateau followed by a post-jet-break-phase and preceded by a plateau or shallow decay may sound the transition of the circum-burst environment from a free-wind to a homogeneous shocked-wind medium.

In this work, a Gaussian structured jet is adopted to fit the late phase of afterglows in GRBs 100814A, 120326A and 120404A. However, we would like to point out that our conclusion about the circum-burst environment (i.e., the free-to-shocked wind environment) in these bursts may be robust. The reasons are shown as follows. Firstly, the late simultaneous bumps found in these bursts are very similar to those in GRB 170817A, which is formed in an off-axis observed external-forward shock propagating in an interstellar medium (Troja et al. 2018; Lamb et al. 2019; Troja et al. 2019; Huang et al. 2019; Ren et al. 2020). This implies that the late bumps in GRBs 100814A, 120326A, and 120404A may be formed in an off-axis observed external-forward shock in a homogeneous medium. Interestingly, there seems to be no plateau/shallow decay in the early phase of GRB 170817A's afterglows (see the figure 1 of Ren et al. 2020, especially the X-ray afterglow in $t_{\text{obs}} \sim 2 - 100$ day). This behavior may also appear in the afterglows of GRBs 120326A and 120404A if their late simultaneous bumps appear with the same mechanism as that in GRB 170817A. In this paradigm, the plateau/shallow decay preceding the bumps in these two bursts may require an another explanation and the external-forward shock in the free-wind environment may be a natural candidate, especially for long GRBs. Secondly, the external-forward shock with other kinds of structured jet are also studied. For example, Huang et al. (2019) has studied the jet structure owing to the jet precession and the corresponding afterglows in a homogeneous environment. Very complex structured jets have been found. Granot et al. (2018) studies the afterglows from 2D relativistic hydrodynamic simulations of a GRB jet propagating in a homogeneous medium. It seems to be the case that the late simultaneous bumps generally appear without preceding by a plateau/shallow decay in the afterglows for a structured jet propagating in a homogeneous medium (e.g., the figures 3 and 5 of Huang et al. 2019, the figures 6 and 7 of Granot et al. 2018). However, our work could not rule out the scenario that other kinds of structured jet propagating only in a homogeneous medium could explain the observed late simultaneous bumps directly followed by a steep decay and preceded by a plateau/shallow decay in these burst. Our scenario, i.e., an off-axis observed structured jet propagating into a free-to-shocked wind environment, only provides a possible way to decipher these bumps.

ACKNOWLEDGMENTS

We thank the anonymous referee for beneficial suggestions that improved the paper. This work is supported by the National Natural Science Foundation of China (grant Nos.11773007, 11503011, 11673006, U1938201, U1731239) and the Guangxi Science Foundation (grant Nos. 2018GXNSFFA281010, 2017AD22006, 2018GXNSFGA281007).

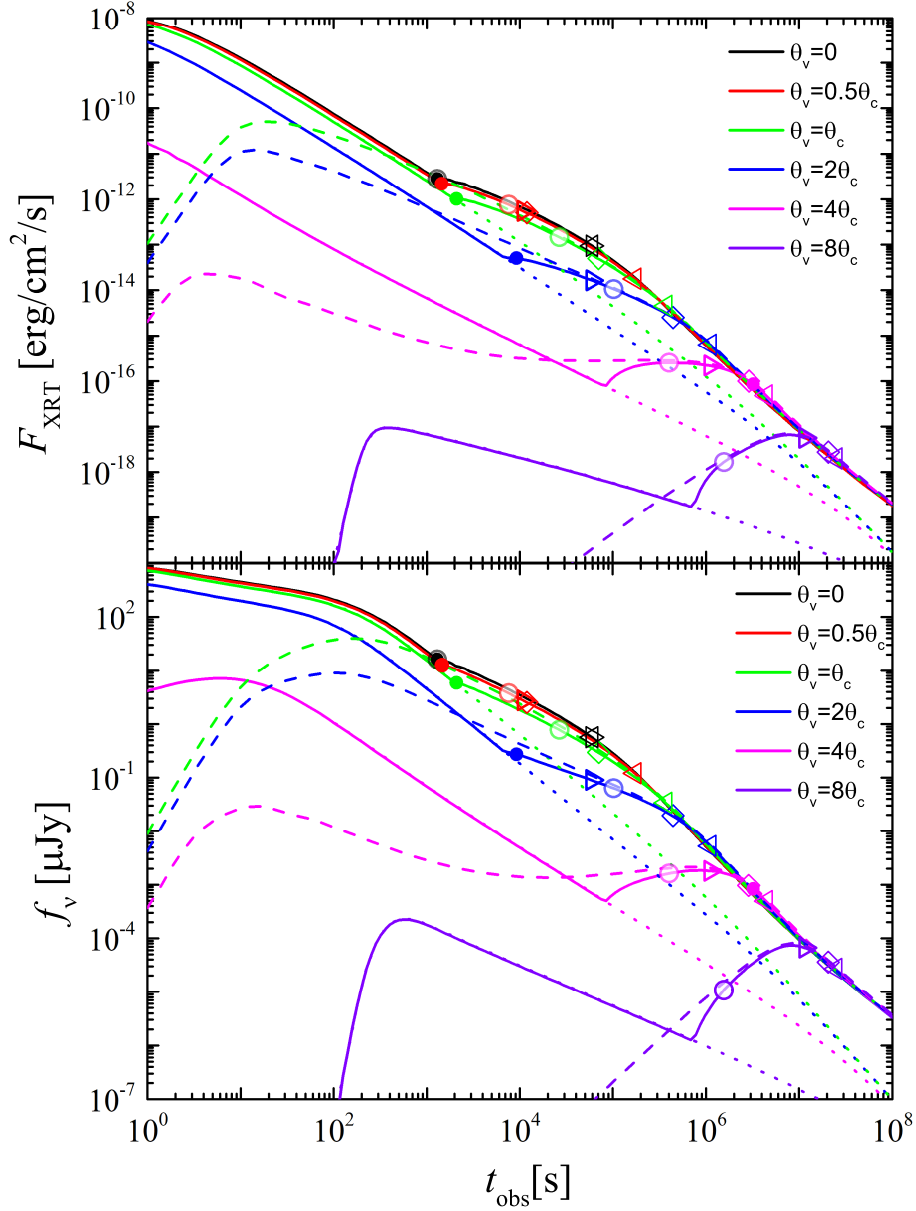


Figure 1. X-ray (top panel, solid lines) and optical (bottom panel, solid lines) light-curves of the external-forward shock in a free-to-shocked wind environment for different viewing angle θ_v , where $E_{k,iso,on} = 10^{52}$ erg, $\Gamma_0 = 250$, $\theta_c = 5^\circ$, $\theta_{jet} = 8\theta_c$, $p = 2.2$, $\epsilon_e = 0.1$, $\epsilon_B = 10^{-4}$, $A_* = 0.01$, $R_{tr} = 10^{17}$ cm, and $z = 1$ are adopted. The dotted/dashed lines represent the afterglows in the pure free/shocked-wind environment with the same parameters as those adopted to calculating the solid lines. The symbols of “●” and “○” represent the observed time for (θ_v, φ_v) -jet and $(0, 0)$ -jet crossing the R_{tr} , respectively. The symbols of “▷”, “◇”, and “◁” represent the observed time of (θ_c, φ_v) -jet, $(0, 0)$ -jet, and $(\theta_c, \varphi_v + \pi)$ -jet beginning to be visible for the observer, respectively. Here, the observed time for (θ_v, φ_v) -jet crossing the R_{tr} for $\theta_v = 8\theta_c$ is significantly larger than 10^8 s and is not plotted in the figure. One can find that the late simultaneous plateaux/bumps appear in the free-to-shocked-wind afterglows. In addition, these late simultaneous bumps/plateaux are directly followed by a post-jet-break-phase and preceded by a shallow decay.

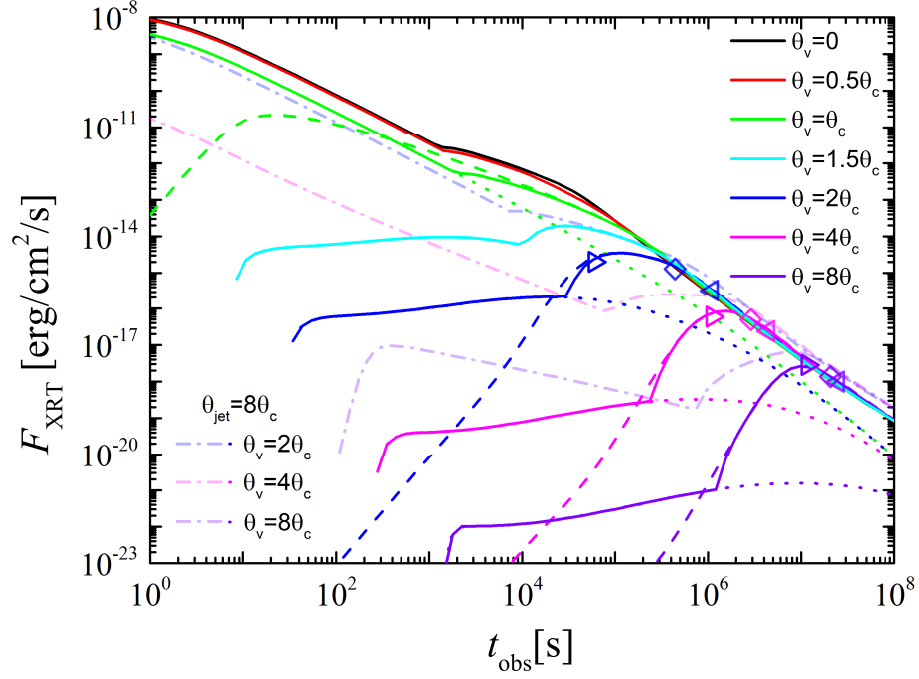


Figure 2. X-ray light-curves (solid/dashed/dotted lines) of the external-forward shock in a free-to-shocked/free/shocked wind environment for different viewing angle θ_v , where the parameters adopted to estimate the emission of the external-forward shock are the same as those in Figure 1 but with $\theta_{\text{jet}} = \theta_c$, and the meanings of “ \triangleright ”, “ \diamond ”, and “ \triangleleft ” symbols are the same as those in Figure 1. For comparison, the solid lines in the top panel of Figure 1 for $\theta_v = 2\theta_c$, $4\theta_c$, and $8\theta_c$ are also plotted with dot-dashed lines in this figure. One can find that the opening angle of the jet may affect the light-curves before the late simultaneous bumps/plateaux.

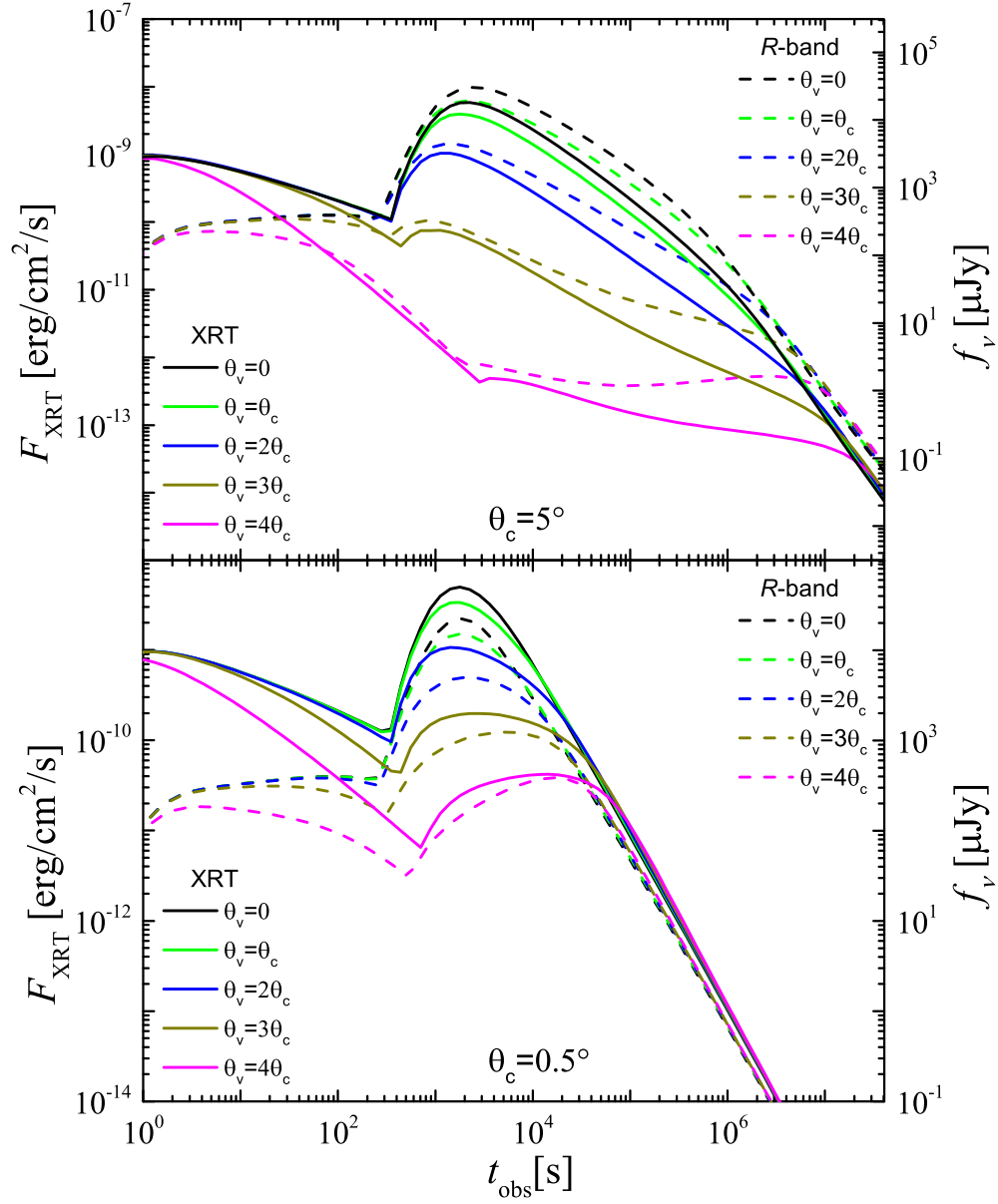


Figure 3. X-ray (solid lines) and optical (dashed lines) light-curves of the external-forward shock in a free-to-shocked wind environment for different viewing angle θ_v , where a structured jet with $E_{k,iso,on} = 10^{55}$ erg, $\Gamma_0 = 100$, $\theta_{jet} = 8\theta_c$, $p = 2.2$, $\epsilon_e = 0.1$, $\epsilon_B = 10^{-4}$, $A_* = 0.01$, $R_{tr} = 10^{17}$ cm, and $\theta_c = 5^\circ$ (top panel) or $\theta_c = 0.5^\circ$ (bottom panel) is adopted. For the given structured jet, the deceleration radius of the on-axis jet flow is beyond the free-wind boundary. It is found that late broad bumps preceded by a long plateau or shallow decay indeed appear in the afterglows for the cases with low viewing angle. In addition, the late broad bump is followed by a normal/steep decay if a structured jet with high/low characteristic angle θ_c (e.g., $\theta_c = 5^\circ/\theta_c = 0.5^\circ$) is adopted.

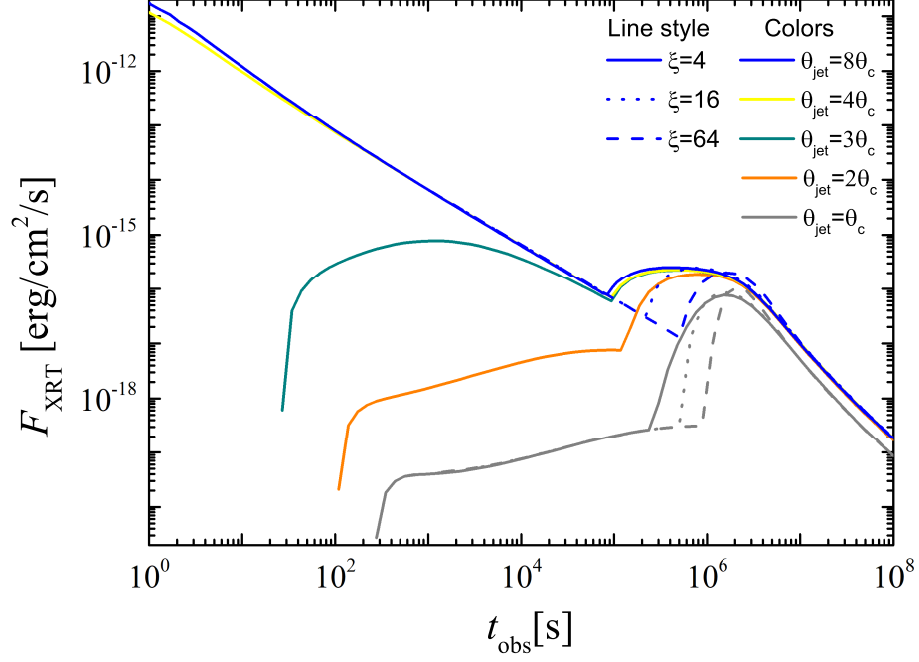


Figure 4. X-ray light-curves (solid lines) of the external-forward shock in a free-to-shocked wind environment for the situations with different θ_{jet} , where $\theta_{\text{jet}} = \theta_c, 2\theta_c, 3\theta_c, 4\theta_c,$ and $8\theta_c$ are adopted. The other parameters adopted to estimate the emission of the external-forward shock are the same as those in Figure 1 and $\theta_v = 4\theta_c$ is set. It reveals that the early phase of the afterglow is shaped by the emission from the jet flow closing to the line of sight and the post-jet-break phase is shaped by the emission from the jet core. To test the effect of the density jump factor ξ on the light-curves, the X-ray afterglows in the situations with $\xi = 16$ (dotted lines) and $\xi = 64$ (dashed lines) for $\theta_{\text{jet}} = 8\theta_c$ or $\theta_{\text{jet}} = \theta_c$ are also shown. It can be found that the transition from the free-wind-phase to the shocked-wind-phase appears later and thus the rise of the bump becomes steeper by increasing the value of ξ .

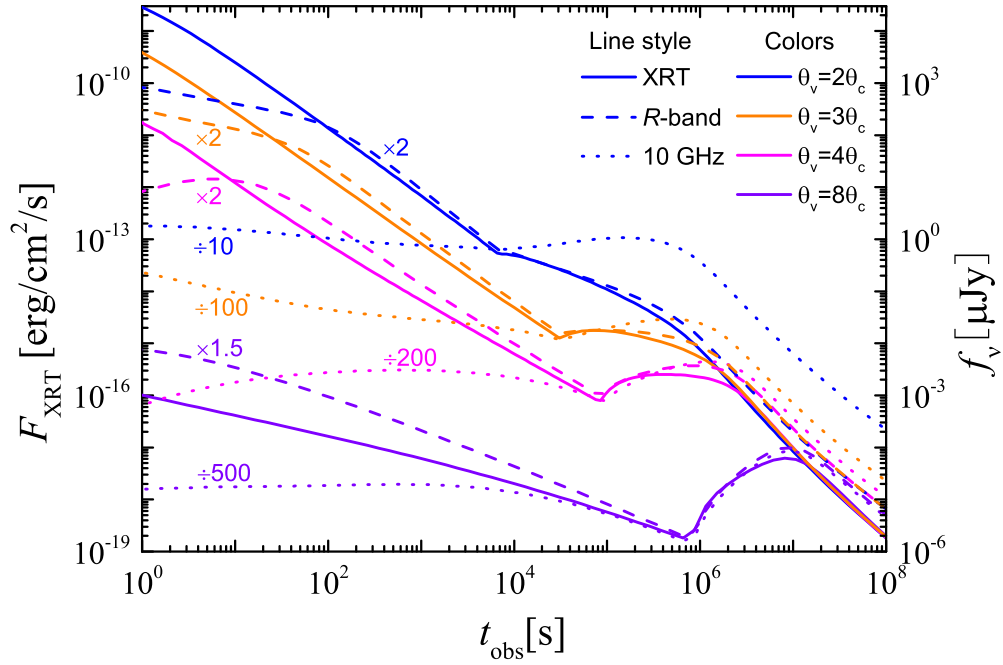


Figure 5. XRT/Optical/Radio afterglows (solid/dashed/dotted lines) from the external-forward shock in a free-to-shocked wind environment for the situations with $\theta_v = 2\theta_c$ (blue lines), $3\theta_c$ (orange lines), $4\theta_c$ (magenta lines) and $8\theta_c$ (violet lines), where the other parameters adopted to estimate the emission of the external-forward shock are the same as those in Figure 1. For comparison, the optical/radio afterglow has been shifted by timing a certain factor. It reveals that the bumps/plateaux in different bands are simultaneous but may be not absolutely achromatic.

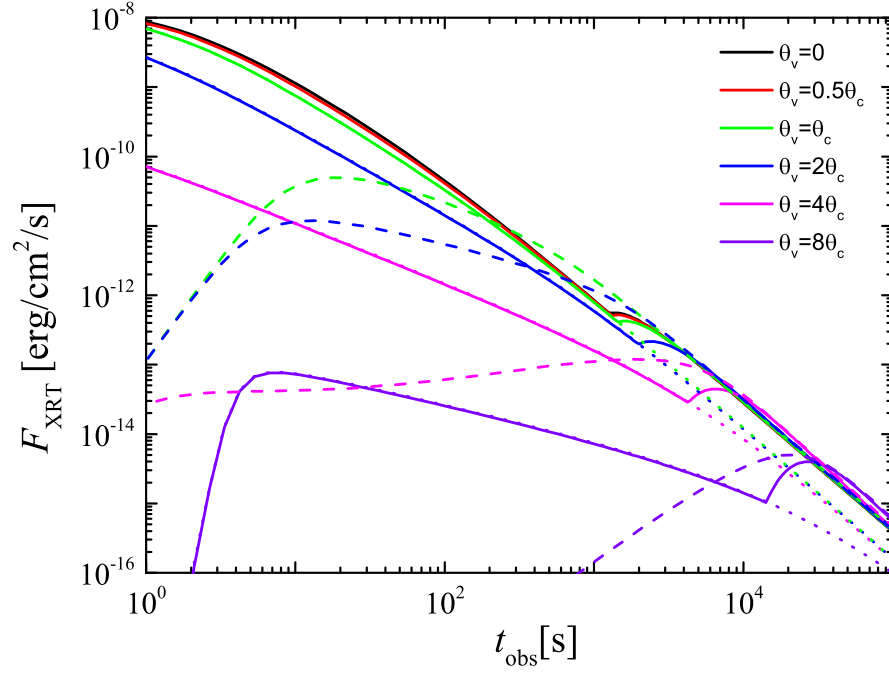


Figure 6. Same as Figure 1 but with $\theta_c = 0.5^\circ$. The width of late bump/plateau which is narrower than that in Figure 1, which reveals that the characteristic angle θ_c of the structured jet may affect the width of the late bump/plateau for a same θ_v/θ_c .

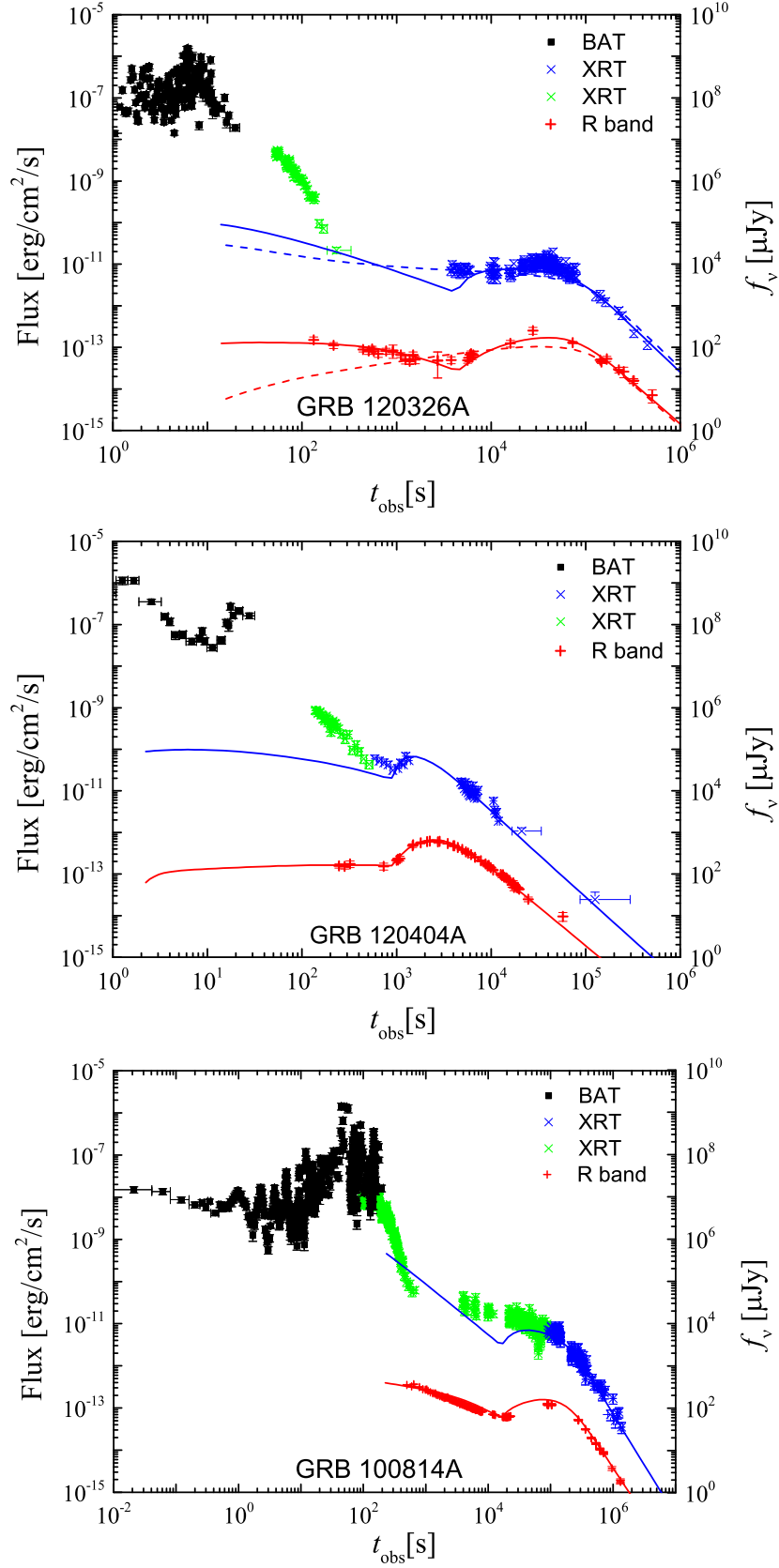


Figure 7. Fitting result of the afterglows in GRB 120326A (top panel), GRB 120404A (middle panel), and GRB 100814A (bottom panel), where blue “ \times ” and red “+” symbols represent the XRT and optical data used in our fittings, respectively. The blue and red lines are the optimal fitting of the late XRT and optical afterglows, respectively.

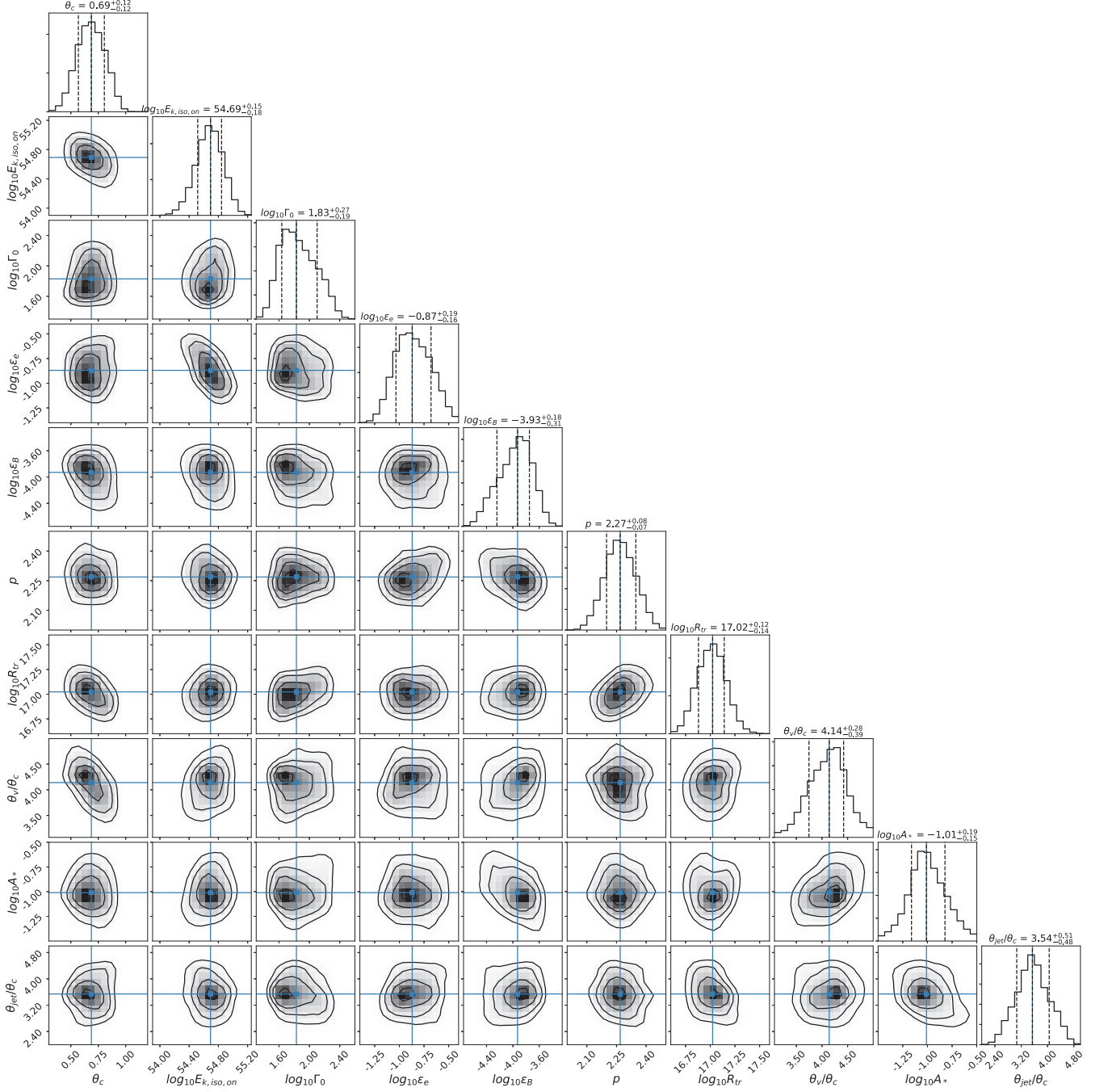


Figure 8. Posterior probability density functions for the physical parameters of the external-forward shock in GRB 120326A from MCMC simulations.

Table 1. Parameters Estimated from the MCMC Sampling

Parameters	GRB 120326A	GRB 120404A	GRB 100814A
θ_c	$0.69^{+0.12}_{-0.12}$	$0.58^{+0.14}_{-0.11}$	$0.89^{+0.12}_{-0.05}$
$\log_{10}(E_{k,\text{iso,on}}/\text{erg})$	$54.69^{+0.15}_{-0.18}$	$53.78^{+0.16}_{-0.14}$	$54.89^{+0.07}_{-0.13}$
$\log_{10}\Gamma_0$	$1.83^{+0.27}_{-0.19}$	$1.86^{+0.03}_{-0.04}$	$2.28^{+0.11}_{-0.09}$
$\log_{10}\epsilon_e$	$-0.87^{+0.19}_{-0.16}$	$-1.01^{+0.12}_{-0.09}$	$-0.51^{+0.01}_{-0.10}$
$\log_{10}\epsilon_B$	$-3.93^{+0.18}_{-0.31}$	$-3.21^{+0.16}_{-0.18}$	$-4.69^{+0.17}_{-0.10}$
p	$2.27^{+0.08}_{-0.07}$	$2.29^{+0.06}_{-0.07}$	$2.60^{+0.04}_{-0.05}$
$\log_{10}(R_{\text{tr}}/\text{cm})$	$17.02^{+0.12}_{-0.14}$	$16.80^{+0.06}_{-0.08}$	$17.60^{+0.07}_{-0.13}$
θ_v/θ_c	$4.14^{+0.28}_{-0.39}$	$0.68^{+0.28}_{-0.25}$	$3.66^{+0.09}_{-0.05}$
$\log_{10}A_*$	$-1.01^{+0.19}_{-0.15}$	$-1.46^{+0.11}_{-0.11}$	$-0.66^{+0.11}_{-0.03}$
$\theta_{\text{jet}}/\theta_c$	$3.54^{+0.51}_{-0.48}$	$1.17^{+0.12}_{-0.10}$	$4.03^{+0.90}_{-0.44}$
E_k/erg	2.23×10^{51}	9.63×10^{49}	5.88×10^{51}

E_k is the total kinetic energy of the structured jet.

APPENDIX

A. ANALYTICAL SOLUTIONS OF THE EXTERNAL-FORWARD SHOCK AND ITS EMISSION

A.1. Analytical Solution for the Dynamics of the External-forward Shock

The emission of the external-forward shock is related to $\gamma'_{e,m}$, $\gamma'_{e,c}$, B' , Γ , and ρ (or R). In addition, the equations of $\gamma'_{e,m} = \epsilon_e(p-2)m_p\Gamma/[(p-1)m_e]$, $\gamma'_{e,c} = 6\pi m_e c/(\sigma_T\Gamma B'^2 t_{\text{obs}}^{\text{on}})$, and $B' = [32\pi\rho(R)\epsilon_B]^{1/2}\Gamma c$ are used to estimate $\gamma'_{e,m}$, $\gamma'_{e,c}$, and B' , respectively. Then, the emission of the external-forward shock at observer time t_{obs} can be estimated only if the dependence of $R = R_{\text{obs}}(\theta, \varphi, \theta_v)$ and $\Gamma_{\text{obs}}(\theta, \varphi, \theta_v) = \Gamma(\theta, R_{\text{obs}})$ on t_{obs} are presented, where R_{obs} and Γ_{obs} are the location and Lorentz factor of the external-forward shock for the (θ, φ) -jet at observer time t_{obs} . The t_{obs} -dependent Γ_{obs} and R_{obs} can be described as

$$\begin{cases} \frac{\Gamma_{\text{obs}}}{\Gamma_0} = \left[1 + \left(\zeta \frac{t_{\text{obs}}}{t_{\text{dec}}} \right)^{3-s} \right]^{\frac{1}{\epsilon+2s-8}}, \\ \frac{R_{\text{obs}}}{R_{\text{dec}}} = \left[1 + \zeta^{\frac{\epsilon-2}{6-2s}} \frac{t_{\text{obs}}}{t_{\text{dec}}} \right]^{\frac{6-2s}{\epsilon+2s-8}} \frac{t_{\text{obs}}}{t_{\text{dec}}}, \\ D = 2\Gamma_0 \left(\frac{\Gamma}{\Gamma_0} \right), \end{cases} \quad \text{for } 2\Gamma\sqrt{\zeta}\sin(\Theta/2) < 1, \quad (\text{A1})$$

and

$$\begin{cases} \frac{\Gamma_{\text{obs}}}{\Gamma_0} = \left[1 + \left(a \frac{t_{\text{obs}}}{t_{\text{dec}}} \right)^{3-s} \right]^{\frac{1}{\epsilon-2}}, \\ \frac{R_{\text{obs}}}{R_{\text{dec}}} = a \frac{t_{\text{obs}}}{t_{\text{dec}}}, \\ D = 2\Gamma_0 a \left(\frac{\Gamma}{\Gamma_0} \right)^{-1}, \end{cases} \quad \text{for } 2\Gamma\sqrt{\zeta}\sin(\Theta/2) > 1, \quad (\text{A2})$$

where the medium mass density with $\rho = \rho_0 R^{-s}$ is adopted and the other parameters are

$$t_{\text{dec}} = (1+z) \frac{R_{\text{dec}}}{2\Gamma_0^2 c}, \quad (\text{A3})$$

$$R_{\text{dec}} = \left[\frac{4\pi\rho_0\Gamma_0(2-\epsilon)}{(3-s)M_0(\theta)} \right]^{1/(s-3)}, \quad (\text{A4})$$

$$\zeta = (\epsilon - 8 + 2s)/(\epsilon - 2), \quad (\text{A5})$$

$$a = 1/[(1 - \cos\Theta)2\Gamma_0^2], \quad (\text{A6})$$

$$t_{\text{obs}}^{\text{on}} \approx \frac{R_{\text{obs}}}{2\Gamma_0^2 c \left[1 + \zeta^{(\epsilon-2)/2} (R_{\text{obs}}/R_{\text{dec}})^{3-s} \right]^{\frac{2}{\epsilon-2}}}. \quad (\text{A7})$$

The derivation of Equations (A1), (A2) and (A7) are presented as follows.

For the (θ, φ) -jet, the evolution of the bulk Lorentz factor in the relativistic regime can be estimated with

$$\frac{m(R)}{M_0(\theta)} = -(\Gamma_0 - 1)^{1/2}(\Gamma_0 + 1)^{1/2-\epsilon} \int_{\Gamma_0}^{\Gamma(\theta,R)} (\gamma - 1)^{-3/2} (\gamma + 1)^{-3/2+\epsilon} d\gamma, \quad (\text{A8})$$

where Γ_0 is the initial Lorentz factor of the fireball. Equation (A8) is obtained based on the following equations (Chiang & Dermer 1999; Piran 1999):

$$\frac{d\Gamma}{dm} = -\frac{\Gamma^2 - 1}{M'}, \quad (\text{A9})$$

$M' = M_0(\theta) + m(R) + U'/c^2$, and $dU' = (1 - \epsilon)(\Gamma - 1)c^2 dm$. Since Equation (A9) fails to reproduce the dynamics in the non-relativistic regime, Huang et al. (1999, 2000) revised Equation (A9) and proposed Equation (3) to more correctly delineate the blastwave dynamics. Then, Equation (A9) is only applied for the relativistic regime. In the relativistic regime, i.e., $\Gamma \gg 1$, Equation (A8) is reduced to

$$\frac{\Gamma}{\Gamma_0} = \left[1 + (2 - \epsilon) \frac{\Gamma_0 m}{M_0} \right]^{\frac{1}{\epsilon - 2}}. \quad (\text{A10})$$

With $m = \int_{R_0}^R r^2 \rho dr \approx \rho_0 R^{3-s}/(3-s)$, one can have

$$\frac{\Gamma}{\Gamma_0} = \left[1 + \left(\frac{R}{R_{\text{dec}}} \right)^{3-s} \right]^{\frac{1}{\epsilon - 2}}. \quad (\text{A11})$$

Based on Equation (A11) and $t_{\text{obs}}^{\text{on}}(\theta, R) = \int_{R_0}^R (c - v) dr / cv$, we can have

$$t_{\text{obs}}^{\text{on}} \approx \begin{cases} \frac{R}{2\Gamma_0^2 c}, & R < R_{\text{dec}}, \\ \frac{\epsilon - 2}{\epsilon - 8 + 2s} \frac{R}{2\Gamma^2 c}, & R \gg R_{\text{dec}}, \end{cases} \quad (\text{A12})$$

and approximately take

$$t_{\text{obs}}^{\text{on}} \approx \frac{R}{2\Gamma_0^2 c \left[1 + \zeta^{(\epsilon-2)/2} (R/R_{\text{dec}})^{3-s} \right]^{\frac{2}{\epsilon-2}}}. \quad (\text{A13})$$

Correspondingly, we can approximately take

$$\frac{R}{R_{\text{dec}}} = \left[1 + \zeta^{\frac{\epsilon-2}{6-2s}} \frac{t_{\text{obs}}^{\text{on}}}{t_{\text{dec}}^{\text{on}}} \right]^{\frac{6-2s}{\epsilon+2s-8}} \frac{t_{\text{obs}}^{\text{on}}}{t_{\text{dec}}^{\text{on}}}, \quad (\text{A14})$$

where t_{dec} is the deceleration time of the (θ, φ) -jet while it moves in the line of sight. With Equation (A14), Equation (A11) can be approximately described as

$$\frac{\Gamma}{\Gamma_0} = \left[1 + \left(\zeta \frac{t_{\text{obs}}^{\text{on}}}{t_{\text{dec}}^{\text{on}}} \right)^{3-s} \right]^{\frac{1}{\epsilon+2s-8}}. \quad (\text{A15})$$

In addition, Equations (5) and (A12) reveal

$$t_{\text{obs}}(\theta, \varphi, \theta_v, R) \approx \begin{cases} (1 - \cos \Theta) R(1+z)/c, & 2\Gamma\sqrt{\zeta} \sin(\Theta/2) > 1, \\ t_{\text{obs}}^{\text{on}}, & 2\Gamma\sqrt{\zeta} \sin(\Theta/2) < 1. \end{cases} \quad (\text{A16})$$

For $2\Gamma\sqrt{\zeta} \sin(\Theta/2) < 1$, Equation (A1) can be easily derived based on Equations (A14), (A15), and (A16). For $2\Gamma\sqrt{\zeta} \sin(\Theta/2) > 1$, one can have $R_{\text{obs}}/R_{\text{dec}} = at_{\text{obs}}/t_{\text{dec}}$ and thus the t_{obs} -dependent Γ can be derived based on Equation (A11).

A.2. $P'(\nu', \theta, R)$ for the (θ, φ) -jet

Assuming the electron energy spectrum as $n'_e(\gamma'_e, \theta, R) = N_{e,\text{tot}}(1-k)(\gamma'_e/\gamma'_{\text{min}})^{-k}/(4\pi\gamma'_{\text{min}})$ at $\gamma'_e \gtrsim \gamma'_{\text{min}} \equiv \min(\gamma'_{e,c}, \gamma'_{e,m})$, one can have

$$P'(\nu', \theta, R) = \left(\frac{\nu'}{\nu'_{\text{min}}} \right)^{1/3} F'_{\nu',\text{max}} \quad \text{for } \nu' < \nu'_{\text{min}} \quad (\text{A17})$$

without considering the synchronization self-absorption effect, where $\nu'_{\text{min}} = \gamma'_{\text{min}}{}^2 q_e B' / (2\pi m_e c)$, $F'_{\nu',\text{max}} = \xi P_{\nu',\text{max}} N_{e,\text{tot}} / (4\pi\Gamma)$ with $\xi = 2.15 \times (3k-3)/(3k-1) \sim 1.5$ for $2 \lesssim k \lesssim 4$, $P_{\nu',\text{max}}(\Gamma_{\text{obs}}, R_{\text{obs}}) = m_e c^2 \sigma_T B' \Gamma / (3q_e)$, and $N_{e,\text{tot}}(R_{\text{obs}}) = 4\pi m / m_p$.

The exact electron spectrum depend on the injection rate Q' , i.e., Equation(8), of electrons from the shock and the cooling effect. Considering only the synchrotron radiation cooling effect, the steady state of electron spectrum can be described as

$$n'_e(\gamma'_e, \theta, R) \propto \begin{cases} \gamma'^{-2}_e, & \gamma'_{e,c} < \gamma'_e < \gamma'_{e,m}, \\ \gamma'^{-(p+1)}_e, & \gamma'_e > \gamma'_{e,m}, \end{cases}$$

for fast cooling (i.e, $\gamma'_{\min} = \gamma'_{e,c} < \gamma'_{e,m}$), and

$$n'_e(\gamma'_e, \theta, R) \propto \begin{cases} \gamma'^{-p}_e, & \gamma'_{e,m} < \gamma'_e < \gamma'_{e,c}, \\ \gamma'^{-(p+1)}_e, & \gamma'_e > \gamma'_{e,c}, \end{cases}$$

for slow cooling (i.e, $\gamma'_{\min} = \gamma'_{e,m} < \gamma'_{e,c}$). Correspondingly, one can have

$$P'(\nu', \theta, R) = \begin{cases} (\nu'/\nu'_c)^{1/3} F'_{\nu,\max}, & \nu' < \nu'_c \\ (\nu'/\nu'_c)^{-1/2} F'_{\nu,\max}, & \nu'_c < \nu' < \nu'_m \\ (\nu'_m/\nu'_c)^{-1/2} (\nu'/\nu'_m)^{-p/2} F'_{\nu,\max}, & \nu' > \nu'_m \end{cases} \quad (\text{A18})$$

for fast cooling, and

$$P'(\nu', \theta, R) = \begin{cases} (\nu'/\nu'_m)^{1/3} F'_{\nu,\max}, & \nu' < \nu'_m \\ (\nu'/\nu'_m)^{-(p-1)/2} F'_{\nu,\max}, & \nu'_m < \nu' < \nu'_c \\ (\nu'_c/\nu'_m)^{-(p-1)/2} (\nu'/\nu'_c)^{-p/2} F'_{\nu,\max}, & \nu' > \nu'_c \end{cases} \quad (\text{A19})$$

for slow cooling, where $\nu'_c = \gamma'^2_{e,c} q_e B' / (2\pi m_e c)$ and $\nu'_m = \gamma'^2_{e,m} q_e B' / (2\pi m_e c)$.

Based on Equations (A18), (A19), (10), and (11), one can estimate the observed total flux density $f_\nu(t_{\text{obs}})$ from the external-forward shock.

A.3. Analytical Light-curves for A Top-hat Jet

In order to estimate the analytical light-curves for a top-hat jet, we assume the radiation energy of the jet shell at radius R are all observed at the same time. For a top-hat jet, the observed flux from the jet shell is mainly dominated by that from the jet flow being close to the line of sight. Then, the location and Lorentz factor of the jet flow being closest to the line of sight at the observer time t_{obs} can be used to depict the emission of the external-forward shock and are represented with \bar{R} and $\bar{\Gamma}$, respectively. With Equations (A18) and (A19), one can have

$$f_\nu(t_{\text{obs}}) = \begin{cases} (\nu/\nu_c)^{1/3} F_{\nu,\max}, & \nu < \nu_c, \\ (\nu/\nu_c)^{-1/2} F_{\nu,\max}, & \nu_c < \nu < \nu_m, \\ (\nu_m/\nu_c)^{-1/2} (\nu/\nu_m)^{-p/2} F_{\nu,\max}, & \nu > \nu_m, \end{cases} \quad (\text{A20})$$

for the fast cooling case, and

$$f_\nu(t_{\text{obs}}) = \begin{cases} (\nu/\nu_m)^{1/3} F_{\nu,\max}, & \nu < \nu_m, \\ (\nu/\nu_m)^{-(p-1)/2} F_{\nu,\max}, & \nu_m < \nu < \nu_c, \\ (\nu_c/\nu_m)^{-(p-1)/2} (\nu/\nu_c)^{-p/2} F_{\nu,\max}, & \nu > \nu_c, \end{cases} \quad (\text{A21})$$

for the slow cooling case, where \textcircled{I} for the situation with $0 \leq \theta_v \lesssim \theta_{\text{jet}}$, $\bar{R} = R_{\text{obs}}(\theta_v, \varphi_v, \theta_v)$, $\bar{\Gamma} = \Gamma_{\text{obs}}(\theta_v, \varphi_v, \theta_v)$, $\nu_m = \nu'_m 2\bar{\Gamma} / (1+z)$, $\nu_c = \nu'_c 2\bar{\Gamma} / (1+z)$, and $F_{\nu,\max} = \kappa(1+z) P_{\nu,\max}(\bar{\Gamma}, \bar{R}) N_{e,\text{tot}}(\bar{R}) / (4\pi d_L^2)$ with $\kappa = \xi \times \{1 - 1/\{1 + 2\bar{\Gamma}^2[1 - \cos(\theta_{\text{jet}} + \theta_v)]\}^2\}$; \textcircled{II} for the situation with $\theta_v > \theta_{\text{jet}} + 1/\bar{\Gamma}$, $\bar{R} = R_{\text{obs}}(\theta_v - \theta_{\text{jet}}, \varphi_v, \theta_v)$, $\bar{\Gamma} = \Gamma_{\text{obs}}(\theta_v - \theta_{\text{jet}}, \varphi_v, \theta_v)$, $\nu_m = \nu'_m / [(1+z)2\bar{\Gamma}]$, $\nu_c = \nu'_c / [(1+z)2\bar{\Gamma}]$, and $F_{\nu,\max} = \kappa(1+z) P_{\nu,\max}(\bar{\Gamma}, \bar{R}) N_{e,\text{tot}}(\bar{R}) / (4\pi d_L^2 \bar{\Gamma}^4)$ with $\kappa = \xi \theta_{\text{jet}} (\pi \sin \theta_v)^{-1} [(\theta_v - \theta_{\text{jet}})^{-4} - (\theta_v + \theta_{\text{jet}})^{-4}]$. The analytical result of \textcircled{I} is consistent with that of Sari et al. (1998).

The expression of $f_\nu(t_{\text{obs}})$ is derived based on Equation (11), where

$$f_\nu(t_{\text{obs}}) \approx \frac{(1+z)}{2d_L^2} P'(\nu \frac{1+z}{2\bar{\Gamma}}, \theta_v, \bar{R}) \int_0^{\theta_{\text{jet}} + \theta_v} D^3 \sin \Theta d\Theta \quad (\text{A22})$$

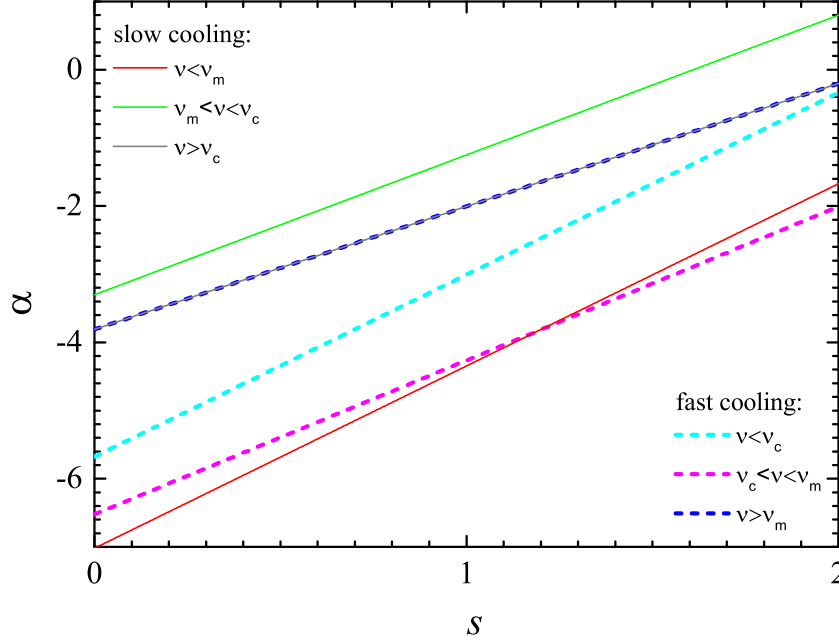


Figure 9. Relation of α and s for an off-axis observer and $\bar{R} > R_{\text{dec}}$, where $f_\nu \propto t_{\text{obs}}^{-\alpha}$ is adopted. One can find that the rise of the free-wind-afterglow is generally gentle compared with that of the shocked-wind-afterglow.

or

$$f_\nu(t_{\text{obs}}) \approx \frac{(1+z)}{d_L^2} \bar{\Gamma} P'(\nu \frac{1+z}{2\bar{\Gamma}}, \theta_v, \bar{R}) \left\{ 1 - \left[\frac{1}{1 + [1 - \cos(\theta_{\text{jet}} + \theta_v)] / (1 - \beta)} \right]^2 \right\} \quad (\text{A23})$$

is obtained for an observer with $0 \leq \theta_v \lesssim \theta_{\text{jet}}$, and

$$f_\nu(t_{\text{obs}}) \approx \frac{(1+z)}{4\pi d_L^2} P'(\nu \frac{1+z}{2\bar{\Gamma}}, \theta_v - \theta_{\text{jet}}, \bar{R}) \left(\frac{2R\theta_{\text{jet}}}{R \sin \theta_v} \right) \int_{\theta_v - \theta_{\text{jet}}}^{\theta_v + \theta_{\text{jet}}} D^3 \sin \Theta d\Theta \quad (\text{A24})$$

or

$$f_\nu(t_{\text{obs}}) \approx \frac{(1+z)}{d_L^2} P'(\nu \frac{1+z}{2\bar{\Gamma}}, \theta_v - \theta_{\text{jet}}, \bar{R}) \frac{1}{\bar{\Gamma}^3} \left(\frac{\theta_{\text{jet}}}{\pi \sin \theta_v} \right) \left[\frac{1}{(\theta_{\text{jet}} - \theta_v)^4} - \frac{1}{(\theta_{\text{jet}} + \theta_v)^4} \right] \quad (\text{A25})$$

is obtained for an observer with $\theta_v > \theta_{\text{jet}} + 1/\bar{\Gamma}$.

In general, the observed spectral flux is expressed as $f_\nu \propto t_{\text{obs}}^{-\alpha} \nu^{-\beta}$ and the so-called ‘‘closure relations’’, i.e., the relationship between the temporal index α and the spectral index β , are discussed (e.g., Zhang & Mészáros 2004; Zhang et al. 2006). With Equations (A1) and (A2), the values of α and β for the situations with $\bar{R} > R_{\text{dec}}$ and $\bar{\Gamma} \gtrsim 3$ are reported in the Table 2, where the situations with $\bar{R} > R_{\text{dec}}$ is related to the normal decay phase and the post-jet-break-phase of afterglows if the GRB is observed on-axis. The relations of α and s for an off-axis observer can be found in Figure 9.

Table 2. The values of α and β in different situations, where $f_\nu \propto t_{\text{obs}}^{-\alpha} \nu^{-\beta}$ is adopted.

Cases	α		
	On-axis before the jet break	Free-wind medium	Shocked-wind medium
Fast cooling	On-axis before the jet break	Free-wind medium	Shocked-wind medium
$\nu < \nu_c$ ($\beta = -\frac{1}{3}$)	$-\frac{3-2s}{\zeta} - 10\frac{3-s}{3(\varepsilon+2s-8)} - \frac{2}{3}$	$\frac{2}{3}$	$-\frac{1}{6}$
$\nu_c < \nu < \nu_m$ ($\beta = \frac{1}{2}$)	$1 - \frac{3}{\zeta} + \frac{3s}{4\zeta}$	$\frac{1}{4}$	$\frac{1}{4}$
$\nu > \nu_m$ ($\beta = \frac{p}{2}$)	$-\frac{12-2s-sp}{4\zeta} - \frac{(3-s)(2p-2)}{\varepsilon+2s-8} + 1$	$-\frac{2-3p}{4} \sim 1.15$	$-\frac{2-3p}{4} \sim 1.15$
Slow cooling	On-axis before the jet break		
$\nu < \nu_m$ ($\beta = -\frac{1}{3}$)	$-\frac{2(3-s)}{3(\varepsilon+2s-8)} - \frac{3}{\zeta} + \frac{4s}{3\zeta}$	0	$-\frac{1}{2}$
$\nu_m < \nu < \nu_c$ ($\beta = \frac{p-1}{2}$)	$-\frac{2p(3-s)}{\varepsilon+2s-8} + \frac{s(p-1)}{4\zeta} - \frac{3}{\zeta} + \frac{3s}{2\zeta}$	$-\frac{1-3p}{4} \sim 1.4$	$-\frac{3(1-p)}{4} \sim 0.9$
$\nu > \nu_c$ ($\beta = \frac{p}{2}$)	$-\frac{(3-s)(2p-2)}{\varepsilon+2s-8} - \frac{3}{\zeta} + \frac{s}{2\zeta} + \frac{sp}{4\zeta} + 1$	$-\frac{2-3p}{4} \sim 1.15$	$-\frac{2-3p}{4} \sim 1.15$
Fast cooling	Off-axis before the jet break		
$\nu < \nu_c$ ($\beta = -\frac{1}{3}$)	$-\frac{2\zeta}{3} - 3 + 2s$	$-\frac{1}{3}$	$-\frac{17}{3}$
$\nu_c < \nu < \nu_m$ ($\beta = \frac{1}{2}$)	$\frac{5(3-s)}{\varepsilon-2} - 3 + \frac{3s}{4} + \zeta$	-2	$-\frac{13}{2}$
$\nu > \nu_m$ ($\beta = \frac{p}{2}$)	$-\frac{12-2s-sp}{4} - \frac{(3-s)(p-6)}{\varepsilon-2} + \zeta$	$-(3-p) \sim -0.8$	$-\frac{16-3p}{2} \sim -4.7$
Slow cooling	Off-axis before the jet break		
$\nu < \nu_m$ ($\beta = -\frac{1}{3}$)	$-3 + \frac{4s}{3} + \frac{8(3-s)}{3(\varepsilon-2)}$	$-\frac{5}{3}$	-7
$\nu_m < \nu < \nu_c$ ($\beta = \frac{p-1}{2}$)	$\frac{s(p+1)}{4} - 3 + s - \frac{(3-s)(p-3)}{(\varepsilon-2)}$	$-(2-p) \sim 0.2$	$-\frac{15-3p}{2} \sim -4.2$
$\nu > \nu_c$ ($\beta = \frac{p}{2}$)	$-\frac{(12-2s-sp)}{4} - \frac{(3-s)(p-6)}{\varepsilon-2} + \zeta$	$-(3-p) \sim -0.8$	$-\frac{16-3p}{2} \sim -4.7$
Fast cooling	Post-jet-break-phase		
$\nu < \nu_c$ ($\beta = -\frac{1}{3}$)	$-\frac{3-2s}{\zeta} - 10\frac{3-s}{3(\varepsilon+2s-8)} - \frac{2}{3} - \frac{2(3-s)}{\varepsilon+2s-8}$	$\frac{7}{6}$	$\frac{7}{12}$
$\nu_c < \nu < \nu_m$ ($\beta = \frac{1}{2}$)	$1 - \frac{3}{\zeta} + \frac{3s}{4\zeta} - \frac{2(3-s)}{\varepsilon+2s-8}$	$\frac{3}{4}$	1
$\nu > \nu_m$ ($\beta = \frac{p}{2}$)	$-\frac{12-2s-sp}{4\zeta} - \frac{(3-s)(2p-2)}{\varepsilon+2s-8} + 1 - \frac{2(3-s)}{\varepsilon+2s-8}$	$-\frac{2-3p}{4} + \frac{1}{2} \sim 1.65$	$-\frac{2-3p}{4} + \frac{3}{4} \sim 1.9$
Slow cooling	Post-jet-break-phase		
$\nu < \nu_m$ ($\beta = -\frac{1}{3}$)	$-\frac{2(3-s)}{3(\varepsilon+2s-8)} - \frac{3}{\zeta} + \frac{4s}{3\zeta} - \frac{2(3-s)}{\varepsilon+2s-8}$	$\frac{1}{2}$	$\frac{1}{4}$
$\nu_m < \nu < \nu_c$ ($\beta = \frac{p-1}{2}$)	$-\frac{2p(3-s)}{\varepsilon+2s-8} + \frac{s(p-1)}{4\zeta} - \frac{3}{\zeta} + \frac{3s}{2\zeta} - \frac{2(3-s)}{\varepsilon+2s-8}$	$-\frac{1-3p}{4} + \frac{1}{2} \sim 1.9$	$-\frac{3(1-p)}{4} + \frac{3}{4} \sim 1.65$
$\nu > \nu_c$ ($\beta = \frac{p}{2}$)	$-\frac{(3-s)(2p-2)}{\varepsilon+2s-8} - \frac{3}{\zeta} + \frac{s}{2\zeta} + \frac{sp}{4\zeta} + 1 - \frac{2(3-s)}{\varepsilon+2s-8}$	$-\frac{2-3p}{4} + \frac{1}{2} \sim 1.65$	$-\frac{2-3p}{4} + \frac{3}{4} \sim 1.9$

 $p = 2.2$ is adopted.

REFERENCES

- Barthelmy, S. D., Cannizzo, J. K., Gehrels, N., et al. 2005, *ApJL*, 635, L133
- Burrows, D. N., Romano, P., Falcone, A., et al. 2005a, *Science*, 309, 1833
- Burrows, D. N., Hill, J. E., Nousek, J. A., et al. 2005b, *SSRv*, 120, 165
- Cannizzo, J. K., Gehrels, N., & Vishniac, E. T. 2004, *ApJ*, 601, 380
- Castor, J., McCray, R., & Weaver, R. 1975, *ApJL*, 200, L107
- Chevalier, R. A., & Li, Z.-Y. 2000, *ApJ*, 536, 195
- Chevalier, R. A., Li, Z.-Y., & Fransson, C. 2004, *ApJ*, 606, 369
- Chiang, J., & Dermer, C. D. 1999, *ApJ*, 512, 699
- Chincarini, G., Moretti, A., Romano, P., et al. 2007, *ApJ*, 671, 1903
- Chincarini, G., Mao, J., Margutti, R., et al. 2010, *MNRAS*, 406, 2113
- De Pasquale, M., Kuin, N. P. M., Oates, S., et al. 2015, *MNRAS*, 449, 1024
- Dyson, J. E., & Williams, D. A. 1997, *The physics of the interstellar medium*, doi:10.1201/9780585368115
- Falcone, A. D., Burrows, D. N., Lazzati, D., et al. 2006, *ApJ*, 641, 1010
- Falcone, A. D., Morris, D., Racusin, J., et al. 2007, *ApJ*, 671, 1921
- Feng, S.-Y., & Dai, Z.-G. 2011a, *Research in Astronomy and Astrophysics*, 11, 1046
- . 2011b, *Research in Astronomy and Astrophysics*, 11, 1046
- Fraija, N., De Colle, F., Veres, P., et al. 2020, *ApJ*, 896, 25
- Fraija, N., Dichiaro, S., Pedreira, A. C. C. d. E. S., et al. 2019, *ApJL*, 879, L26
- Fraija, N., Veres, P., Zhang, B. B., et al. 2017, *ApJ*, 848, 15
- García-Segura, G., Langer, N., & Mac Low, M. M. 1996, *A&A*, 316, 133
- Gehrels, N., Chincarini, G., Giommi, P., et al. 2004, *ApJ*, 611, 1005
- Geng, J.-J., Huang, Y.-F., Wu, X.-F., Zhang, B., & Zong, H.-S. 2018, *ApJS*, 234, 3
- Geng, J. J., Wu, X. F., Huang, Y. F., Li, L., & Dai, Z. G. 2016, *ApJ*, 825, 107
- Gorbovsokoy, E. S., Lipunova, G. V., Lipunov, V. M., et al. 2012, *MNRAS*, 421, 1874
- Granot, J., Gill, R., Guetta, D., & De Colle, F. 2018, *MNRAS*, 481, 1597
- Granot, J., Miller, M., Piran, T., Suen, W. M., & Hughes, P. A. 2001, in *Gamma-ray Bursts in the Afterglow Era*, ed. E. Costa, F. Frontera, & J. Hjorth, 312
- Guidorzi, C., Mundell, C. G., Harrison, R., et al. 2014, *MNRAS*, 438, 752
- Hou, S. J., Geng, J. J., Wang, K., et al. 2014, *ApJ*, 785, 113
- Huang, B.-Q., Lin, D.-B., Liu, T., et al. 2019, *MNRAS*, 487, 3214
- Huang, L.-Y., Wang, X.-G., Zheng, W., et al. 2018, *ApJ*, 859, 163
- Huang, Y. F., Dai, Z. G., & Lu, T. 1999, *MNRAS*, 309, 513
- Huang, Y. F., Gou, L. J., Dai, Z. G., & Lu, T. 2000, *ApJ*, 543, 90
- Jin, Z. P., Xu, D., Covino, S., et al. 2009a, *MNRAS*, 400, 1829
- . 2009b, *MNRAS*, 400, 1829
- Kamble, A., Resmi, L., & Misra, K. 2007, *ApJL*, 664, L5
- Kong, S. W., Wong, A. Y. L., Huang, Y. F., & Cheng, K. S. 2010, *MNRAS*, 402, 409
- Kumar, P., Hernández, R. A., Bošnjak, Ž., & Barniol Duran, R. 2012, *MNRAS*, 427, L40
- Lamb, G. P., Lyman, J. D., Levan, A. J., et al. 2019, *ApJ*, 870, L15
- Laskar, T., Berger, E., Margutti, R., et al. 2015, *ApJ*, 814, 1
- Li, L., Liang, E.-W., Tang, Q.-W., et al. 2012, *ApJ*, 758, 27
- Li, L., Wang, X.-G., Zheng, W., et al. 2020, *ApJ*, 900, 176
- Liang, E. W., Zhang, B., O'Brien, P. T., et al. 2006, *ApJ*, 646, 351
- Liang, E.-W., Li, L., Gao, H., et al. 2013, *ApJ*, 774, 13
- Lin, D.-B., Mu, H.-J., Liang, Y.-F., et al. 2017a, *ApJ*, 840, 118
- Lin, D.-B., Mu, H.-J., Lu, R.-J., et al. 2017b, *ApJ*, 840, 95
- Marshall, F. E., Antonelli, L. A., Burrows, D. N., et al. 2011, *ApJ*, 727, 132
- Melandri, A., Virgili, F. J., Guidorzi, C., et al. 2014, *A&A*, 572, A55
- Mészáros, P., & Rees, M. J. 1999, *MNRAS*, 306, L39
- Mu, H.-J., Gu, W.-M., Hou, S.-J., et al. 2016a, *ApJ*, 832, 161
- Mu, H.-J., Lin, D.-B., Xi, S.-Q., et al. 2016b, *ApJ*, 831, 111
- Nardini, M., Elliott, J., Filgas, R., et al. 2014, *A&A*, 562, A29
- Nousek, J. A., Kouveliotou, C., Grupe, D., et al. 2006, *ApJ*, 642, 389
- O'Brien, P. T., Willingale, R., Osborne, J., et al. 2006, *ApJ*, 647, 1213
- Panaitescu, A., Mészáros, P., Burrows, D., et al. 2006, *MNRAS*, 369, 2059
- Panaitescu, A., & Vestrand, W. T. 2011, *MNRAS*, 414, 3537
- Pe'er, A., & Wijers, R. A. M. J. 2006, *ApJ*, 643, 1036
- Piran, T. 1999, *PhR*, 314, 575

- Racusin, J. L., Oates, S. R., Schady, P., et al. 2011, *ApJ*, 738, 138
- Ramirez-Ruiz, E., Dray, L. M., Madau, P., & Tout, C. A. 2001, *MNRAS*, 327, 829
- Ren, J., Lin, D.-B., Zhang, L.-L., et al. 2020, *ApJL*, 901, L26
- Romano, P., Moretti, A., Banat, P. L., et al. 2006, *A&A*, 450, 59
- Sari, R., & Piran, T. 1999a, *ApJL*, 517, L109
- . 1999b, *ApJ*, 520, 641
- Sari, R., Piran, T., & Narayan, R. 1998, *ApJL*, 497, L17
- Scalo, J., & Wheeler, J. C. 2001, *ApJ*, 562, 664
- Troja, E., Piro, L., Ryan, G., et al. 2018, *MNRAS*, 478, L18
- Troja, E., van Eerten, H., Ryan, G., et al. 2019, *MNRAS*, 2169
- Urata, Y., Huang, K., Takahashi, S., et al. 2014, *ApJ*, 789, 146
- van Eerten, H., Zhang, W., & MacFadyen, A. 2010, *ApJ*, 722, 235
- van Eerten, H. J., & MacFadyen, A. I. 2012, *ApJ*, 751, 155
- Wang, X.-G., Zhang, B., Liang, E.-W., et al. 2015, *ApJS*, 219, 9
- Weaver, R., McCray, R., Castor, J., Shapiro, P., & Moore, R. 1977, *ApJ*, 218, 377
- Wu, X.-F., Hou, S.-J., & Lei, W.-H. 2013, *ApJL*, 767, L36
- Yi, S.-X., Lei, W.-H., Zhang, B., et al. 2017, *Journal of High Energy Astrophysics*, 13, 1
- Yi, S.-X., Wu, X.-F., Wang, F.-Y., & Dai, Z.-G. 2015, *ApJ*, 807, 92
- Yi, S.-X., Xi, S.-Q., Yu, H., et al. 2016, *ApJS*, 224, 20
- Yu, Y. B., Huang, Y. F., Wu, X. F., Xu, M., & Geng, J. J. 2015, *ApJ*, 805, 88
- Zhang, B., Fan, Y. Z., Dyks, J., et al. 2006, *ApJ*, 642, 354
- Zhang, B., & Mészáros, P. 2004, *International Journal of Modern Physics A*, 19, 2385
- Zhang, B.-B., Liang, E.-W., & Zhang, B. 2007, *ApJ*, 666, 1002
- Zhang, W., & MacFadyen, A. 2009, *ApJ*, 698, 1261